

A study of streamwise vortex structure in a stratified shear layer

By DAVID G. SCHOWALTER†, CHARLES W. VAN ATTA‡
AND JUAN C. LASHERAS

Department of Applied Mechanics and Engineering Sciences 0411, University of California,
San Diego, La Jolla, CA 92093, USA.

(Received 26 November 1993 and in revised form 15 July 1994)

The existence of an organized streamwise vortical structure, which is superimposed on the well known coherent spanwise vorticity in nominally two-dimensional free shear layers, has been studied extensively. In the presence of stratification, however, buoyancy forces contribute to an additional mechanism for the generation of streamwise vorticity. As the spanwise vorticity layer rolls up and pulls high-density fluid above low-density fluid, a local instability results. The purpose of the current investigation is to force the three-dimensional instability in the stratified shear layer. In this manner, we experimentally observe the effect of buoyancy on the streamwise vortex tube evolution, the evolution of the buoyancy-induced instability, and the interaction between these two vortical structures. A simple numerical model is proposed which captures the relevant physics of the flow evolution. It is found that, depending on the location, streamwise vortices resulting from vortex stretching may be weakened or enhanced by the stratification. Buoyancy-induced vortex structures are shown to form where the unstable part of the interface is tilted by the streamwise vortex tubes. These vortices strengthen initially, then weaken downstream, the timescale for this process depending upon the degree of stratification. For initial Richardson numbers larger than about 0.03, the baroclinically weakened vortex tubes eventually disappear as the flow evolves downstream and the baroclinically generated vortices dominate the three-dimensional flow structure.

1. Introduction

It is of value to study geophysical flows to understand the world around us, and there are also important practical aspects. Recently, there has been increased awareness of the effects of industry on the ecosystem of the planet. If a pollutant is introduced into the atmosphere or a body of water, it is important that we understand how that pollutant dilutes, or mixes. It is currently believed that we can determine whether or not the mean temperature of the Earth is rising by measuring the sound speed through the ocean. This sound speed depends on the the temperature of the deep ocean, which in turn depends on the heat flux from the surface layer, and hence, the mixing across the thermocline.

Identification of mixing mechanisms in the atmosphere and the upper ocean continues to be a difficult task. One contributing mechanism of turbulence generation

† Current address: Department of Marine, Earth and Atmospheric Science, Box 8208, North Carolina State University, Raleigh, NC 27695, USA.

‡ Also Scripps Institution of Oceanography.

results from the amplification of the Kelvin–Helmholtz instability, which arises in a region of strong shear surrounded by regions of low shear. The overturns which result from this initial instability are usually referred to as Kelvin–Helmholtz billows, Kelvin–Helmholtz cores, or rollers. A number of observations support the existence of this type of instability in the ocean.

Woods (1968) made temperature and dye visualization measurements in the summer thermocline in the Mediterranean Sea near Malta. He observed a step structure in the vertical temperature profile in which roughly 4 m thick layers were separated by thin regions of high temperature gradient and strong velocity gradient. Flow visualization through dye injection revealed that internal wave shear and drift shear between layers often cancelled, but sometimes added to create an instability of the Kelvin–Helmholtz type. These would grow to a height of about one quarter of their wavelength, then break. Woods made a simple two-layer model, and found that the sheet would indeed become unstable if drift and wave shear were added. The entrainment during these sporadic events was so much larger than that associated with the weak turbulence of the layers, that the heat flux was controlled by the frequency of these instabilities. Orlanski & Bryan (1969) suggested that the step structure seen by Woods is *created* by a convective instability as opposed to the shear instability he observed. The energy required for shear instability is about four times that required for convective instability. Therefore, the shear instability probably arises after the step structure is formed.

Marmorino (1987) measured the fine structure in the thermocline and found ‘Kelvin–Helmholtz type’ structures with wavelengths between 50 and 80 m. Their height-to-length aspect ratios were between 0.06 and 0.11. It was impossible to say whether these were actually Kelvin–Helmholtz billows, but the observations were consistent with those made by Thorpe *et al.* (1977) in Loch Ness and billow sizes were what one would expect given the initial shear layer thickness.

Perhaps the most striking observation of these structures in the ocean took place in the Strait of Gibraltar. The flow in this strait consists of cold, low-salinity water flowing eastward over westward flowing, warm, high-salinity water. Farmer & Armi (1988) took acoustic image measurements along with instantaneous velocity, temperature, and salinity measurements. The acoustic images clearly showed Kelvin–Helmholtz rollers. In addition, the region of maximum shear was displaced vertically from the region of maximum density gradient, showing that, in nature, there can be an asymmetry in flows in which the Kelvin–Helmholtz instability occurs.

The fundamental dynamics of these diverse geophysical flows are retained by studying the stably stratified free shear layer. In this limit, there are two layers in shear such that the interface initially lies perpendicular to the gravity vector and the higher-density fluid lies below the lower-density fluid. A great deal of work has been done on the evolution of unstratified free shear layers. The groundbreaking work was accomplished by Liepmann & Laufer (1947), who measured mean velocity profiles, turbulence levels, Reynolds stresses, and correlation coefficients. Through observations in a low Reynolds number shear layer, Winant & Browand (1974) proposed that most of the entrainment of non-turbulent fluid into the shear layer takes place when the vortical structures resulting from the Kelvin–Helmholtz instability pair and amalgamate. This process continues downstream, so that the number of vortices per streamwise distance gradually decreases while the size of a vortex gradually increases. Brown & Roshko (1974) showed that Kelvin–Helmholtz rollers control the dynamics of the turbulence even at Reynolds numbers (Ux/ν) up to 0.5×10^6 . Dimotakis

& Brown (1976) observed similar dynamics of the Kelvin–Helmholtz structures at Reynolds numbers up to 3×10^6 .

Konrad (1976) measured concentration in a gas shear layer. He found that the amount of mixing at the molecular scale was very small until a critical Reynolds number was reached, at which point the molecular mixing was enhanced, this phenomenon being termed the mixing transition. Breidenthal (1981) performed an experiment on a chemically reacting mixing layer. The flow contained a pH indicator which would only be visualized in regions that were mixed at the molecular scale. He noted that there was very little mixing in the shear layer until the downstream point at which three-dimensionality of the rollers became visible. The first hint of this three-dimensionality was a ‘wiggle’ or spanwise sinuous disturbance in the vortices. Jimenez (1983) observed spanwise structure and noticed that changes in initial conditions changed the positions of spanwise structures. Bernal & Roshko (1986) further investigated the three-dimensionality of the turbulent mixing layer. They used shadowgraph visualization in a gas facility and laser-induced fluorescence in a water facility, observing streamwise streaks or vortices in both flows. Changes in screens in the turbulence management section of the facilities produced changes in the streak positions. As shown theoretically by Lin & Corcos (1984), the stretching in the braid region between the spanwise vortex cores can lead to enhancement of spanwise vorticity which is perturbed to have a component in the streamwise direction. Lasheras & Choi (1988) introduced sinusoidal spanwise forcing at the end of the splitter plate and thus observed the development of the streamwise vortex structure with a single, well defined spanwise wavelength. Their results supported the mechanism proposed by Lin & Corcos and, furthermore, they observed that after vortex enhancement by stretching, vorticity is pulled more strongly into the streamwise direction until there are a series of hairpins extending from the underside of one roller to the top of its neighbour. The distortion of spanwise braid vorticity is 180° out of phase with the distortion of the cores. By direct numerical simulation, Rogers & Moser (1992) confirmed these findings, as well as observing the concentration of spanwise core vorticity into ‘cup’ regions between the streamwise vortex tubes. To apply all of these studies to the ocean and the atmosphere, one must look at the effect of stratification.

The developing stratified shear layer was studied experimentally by Browand & Winant (1973) and by Koop & Browand (1979). After collapse of the Kelvin–Helmholtz cores, Browand & Winant observed an additional mode of instability called the Holmboe mode. This occurs in high Richardson number shear layers in which the shear region is larger than twice the thickness of the density interface. For Richardson numbers ($Ri_0 = g(\Delta\rho/\rho)\theta_0/(\Delta U)^2$) less than about 0.15, Koop & Browand observed active turbulent growth with coherent Kelvin–Helmholtz structures. The structures paired, leading to thickening of the shear layer. Eventually, fragmentation, decay, and relaminarization occurred when there was insufficient available energy for growth to continue. For Richardson numbers greater than 0.15, Holmboe interfacial waves grew in the initial region and broke at their crests. Relaminarization did not occur for this case in their apparatus.

Gartrell (1979) took numerous statistical measurements in a large-scale stratified shear layer. Restratification and collapse led to large mean shear in the downstream flow relative to similar unstratified flows. One conclusion was that there was a great deal of difficulty in relating bulk mixing rates to bulk flow properties without considering fine-scale structure and the associated energy transfer.

Lawrence *et al.* (1987) compared a linear stability analysis of Kelvin–Helmholtz modes with experimental observations using fluorescent dye. An important parameter

in their investigation was the asymmetry parameter ($\epsilon = 2d/h$), where h is the slope thickness of the initial velocity profile, and d is the separation between the centres of the velocity profile and the density profile. For $\epsilon > 1$ (meaning the centre of the density interface is initially below or above the strongly sheared region), they showed that the Holmboe mode disappears from the initial growth region. Rollers were observed to detach from the lower layer in some cases, and some spanwise variation due to gravitational instability was also observed. The Holmboe mode was again observed downstream after collapse of the Kelvin–Helmholtz cores, since the mixing due to collapse reduces ϵ .

A two-dimensional numerical study of the nonlinear development of stratified shear layers was undertaken by Patnaik, Sherman & Corcos (1976). They discovered that gravitational stability stunts the growth of rollers when the Richardson number is well below 0.25, the value at which the shear layer becomes stable. Changing the wavelength and the initial Richardson number greatly altered the appearance of the cores. They saw no secondary, smaller-scale instabilities, which they attributed to their low maximum Reynolds number of 200. Relaxation of the core occurred by damped oscillations and smearing of the density field through diffusion.

Statically unstable regions are created in Kelvin–Helmholtz billows as concentrated vorticity carries heavy fluid above light fluid. This results in a three-dimensional instability mode related to the Rayleigh–Taylor instability, in which vortices are created by the baroclinic production term in the variable-density vorticity transport equation. Klaassen & Peltier (1985*a*) numerically studied the linear range of this instability. They noted that the work of Patnaik *et al.* had been purely two-dimensional and cited that as the reason for lack of observed small-scale structure. Their stability analysis assumed that the two-dimensional roll-up timescale was much greater than the three-dimensional disturbance timescale. The Reynolds number was chosen to be between 300 and 900 and they used an initial Richardson number of 0.07. Unstable modes consisted of real eigenvalues corresponding to exponential growth, and complex conjugate pairs corresponding to oscillating stationary waves. The largest growth was associated with the real eigenvalues. Each time a core overturns, a new unstable region is created. Klaassen & Peltier referred to these as super-adiabatic regions (SAR). Growth rates for a given Reynolds number were highest for spanwise disturbances in the primary SAR, the first to form. Klaassen & Peltier (1991) studied the effect of Richardson number on stability using the same formulation. They discovered that the highest growth rates occurred for Richardson numbers between 0.08 and 0.12.

Thorpe (1985) created an unsteady shear layer with a tilting tank. The tank was filled with a layer of brine below a layer of fresh water. As the tank was tilted at a small angle, the layers moved in opposite directions. The two layers had different indices of refraction, so the flow could be visualized via the shadowgraph technique. He observed a number of three-dimensional instabilities, including those discussed in detail by Lasheras & Choi, helical pairing of Kelvin–Helmholtz billows, and the convective instabilities studied by Klaassen & Peltier. The latter appeared as longitudinal rolls. $r = \lambda_c/\lambda_{KH}$ varied between 0.15 and 0.05 for Reynolds numbers between 300 and 1500, where λ_c is the wavelength of the convective rolls and λ_{KH} is the Kelvin–Helmholtz wavelength. The ratio decreased monotonically with Reynolds number. Within experimental error, these data were in agreement with theoretical predictions made by Klaassen & Peltier (1985*b*).

Three-dimensional numerical simulations of stratified shear layer development have been done by Staquet (1989) and Staquet & Riley (1989). Staquet found that baroclinic

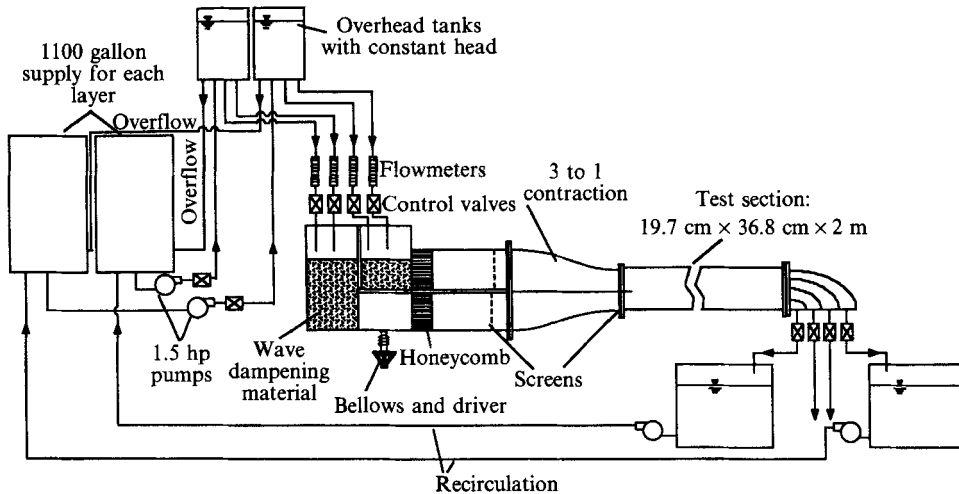


FIGURE 1. Flow facility used for experiments.

effects became very important in the production of spanwise vorticity in the braid region between the spanwise cores. Under certain conditions, that region became unstable to secondary spanwise Kelvin–Helmholtz modes. Staquet & Riley noticed a ‘wave-breaking’ type of spanwise collapse of the core, the wavelength being forced by their periodic boundary conditions. The relationship of this collapse to baroclinic production of streamwise vorticity or to the work of Klaassen & Peltier remains unclear.

The purpose of the current investigation was to force the three-dimensional instability in the stratified shear layer. In this manner, we could observe experimentally the effect of buoyancy on the streamwise vortex tube evolution, the evolution of the buoyancy-induced instability, and any interaction between vorticity concentrations resulting from these two effects. In addition, we have constructed a simple phenomenological numerical model to illustrate the essential physics describing the effect of buoyancy on streamwise vortex tube evolution and the presently observed creation of streamwise vorticity by buoyancy. We experimentally investigate the effect of changing the initial Richardson number but not the velocity ratio or the symmetry parameter, ϵ . Experimental methods and apparatus are discussed in §2 while §3 contains experimental results and discussion of those results. The numerical modeling is described and discussed in §4 and conclusions are in §5.

2. Experimental methods and apparatus

2.1. Two-layer shear channel

The flow facility used for the experiments is shown schematically in figure 1. Each layer has an independent supply, flow rate control, and turbulence management section. A splitter plate separates the two streams which meet in an open channel test section. The existence of a free surface here minimizes the streamwise pressure gradient, and each layer has an aspect ratio of 3.74, thus avoiding three-dimensional wall effects for the present experiments.

The frequency of the Kelvin–Helmholtz instability can be forced with the bellows and driver shown below the lower-layer inlet section. The driver consists of a

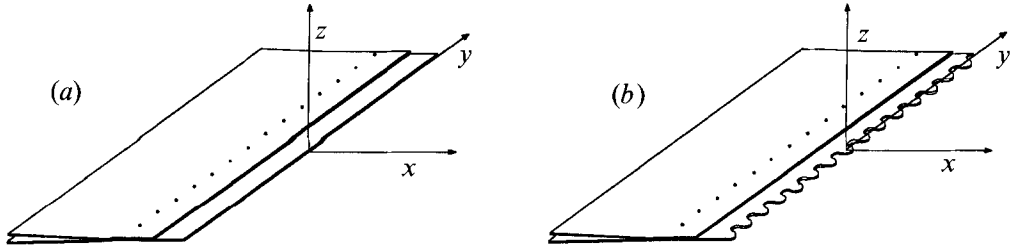


FIGURE 2. Splitter plate tips used in experiments. (a) Flat splitter plate trailing edge. (b) Indented splitter plate trailing edge.

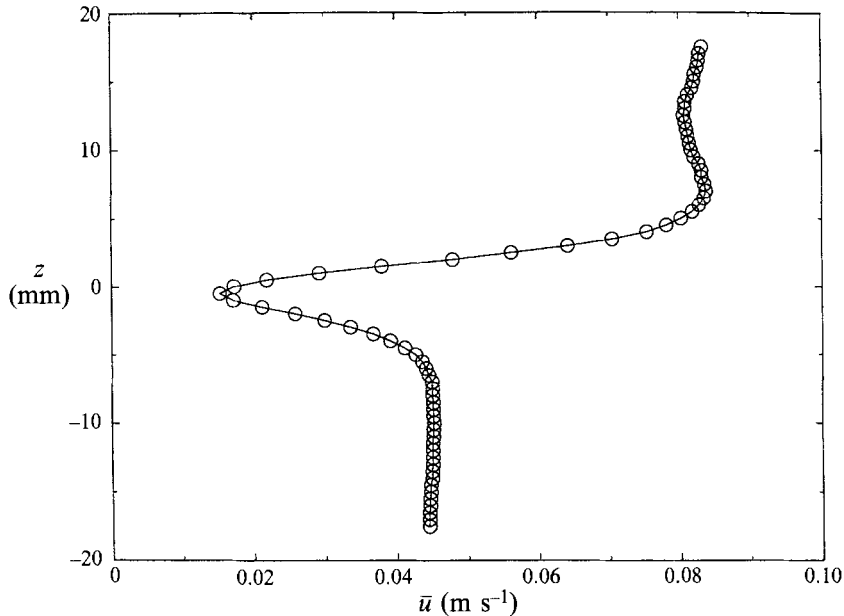
speaker whose cone is connected to a bellows with the upper end open to the inlet section. The speaker is driven with a signal generator and an amplifier. To enable the phase-averaging of measurements, the shear layer roll-up was forced at the observed natural frequency (2.03 Hz), the mechanism producing a sinusoidal free stream velocity fluctuation with an r.m.s. value of roughly 2.5% of the mean bottom layer velocity. This amplitude of the forcing was chosen based upon qualitative visual observation to achieve the most nearly periodic and repeatable flow. Without this forcing, growth rates of spanwise Kelvin–Helmholtz vortices and streamwise vortices would be smaller. Our purpose, however, was not to duplicate precisely what occurs in nature, but to have a dominant wavenumber in the perturbation spectrum, enabling a clear understanding of the dynamics.

Two splitter plate trailing edges were used in the course of this study, both of which are shown in figure 2, along with axis definitions. The first was a straight trailing edge and the second had a spanwise sinusoidal perturbation for forcing the three-dimensional instability. The same type of splitter plate tip was used by Lasheras & Choi to force the three-dimensional instability in the unstratified case. For all experiments in this study for which the indented splitter plate was used, the amplitude of the perturbation was 0.3 cm and the wavelength was 2.4 cm. The wavelength was chosen to be large enough to avoid interaction between structures in separate spanwise periods, while the amplitude of the perturbation was chosen to achieve repeatable results. Note that we have chosen x to represent the streamwise direction, y to represent the spanwise direction, and z to represent the vertical direction.

For all experiments presented in this paper, the upper-layer velocity was set to 8.2 cm s^{-1} and the lower layer was set to 4.5 cm s^{-1} . Figure 3 shows the velocity profile at a downstream position of 1.3 cm. The velocities were measured with a laser-Doppler anemometer, which will be discussed in §2.4. The boundary layers from the top and bottom of the splitter plate can be observed clearly. An initial lengthscale is required to calculate initial Richardson numbers and Reynolds numbers. Koop & Browand used the integral lengthscale,

$$\theta_0 = \int_{-\infty}^{\infty} \left[\frac{1}{4} - \left(\frac{u_0(z) - \bar{U}}{\Delta U} \right)^2 \right] dz, \quad (2.1)$$

where ΔU is the difference in the velocities of the two free streams, $u_0(z)$ is the initial mean velocity profile, and \bar{U} is the average of the free stream velocities. That integral assumes, however, that the value of $u_0(z)$ is always between the two free

FIGURE 3. Initial velocity profile, $x=1.3$ cm.

stream velocities. In order to use a lengthscale which will be compatible with past investigators, we have chosen to use the same integral lengthscale, but with $u_0(z)$ representing a fictitious linear velocity profile between the free streams. The linear profile was chosen to meet the free stream value at the z -position at which the experimental mean velocity reaches 99% of the free stream value. For the profile shown here, this results in a thickness of $\theta_0 = 0.20$ cm, giving us an initial Reynolds number ($Re_0 = \Delta U \theta_0 / \nu$) of 87. The overall Reynolds number ($\Delta U \theta_{vis} / \nu$) in the region in which the bulk of the measurements were taken was about 650, where θ_{vis} refers to the visual thickness further discussed in §3.2.

Past investigators (e.g. Koop & Browand 1979) calculated a lengthscale at a downstream position at which the wake component had been removed by viscosity. Owing to the forcing in this case, however, it was not possible to measure profiles further downstream without the interference of the Kelvin–Helmholtz rollers. We believe that the lengthscale, however, remains valid for comparison with previous results, since it represents the overall thickness of the initial sheared region. Nonetheless, it should be stressed to the reader that the Reynolds number and the Richardson number (§2.2) are not explicitly measured, since θ_0 is an estimated quantity.

The exit of the channel contained four layers. The middle two layers contained mixed fluid and this was discarded. When the flow was stratified, the shear layer never grew to be larger than the thickness of those two layers. Therefore, the unmixed fluid in the top and bottom exit layers was recirculated. This had no effect on the density profile. One experiment lasted for about 20 min, after which the water supply was exhausted.

2.2. Density stratification

The initial Richardson number for shear layer experiments is traditionally defined as

$$Ri_0 = \frac{g(\Delta\rho/\rho_0)\theta_0}{(\Delta U)^2}, \quad (2.2)$$

where $\Delta\rho$ is the density difference between the two layers, ρ_0 is the mean density, g is the gravitational acceleration, and ΔU is the velocity difference between the layers. The Richardson number was varied in these experiments by changing the density difference alone. All other parameters remained constant from one experiment to the next. In preliminary experiments from which shear layer growth was calculated, the density difference was accomplished by adding ordinary table salt to the lower layer. In later experiments, it was necessary for each layer to have the same refractive index, but different densities, enabling the use of laser-Doppler anemometry in a stratified flow. To accomplish this, we dissolved magnesium sulphate in the lower layer and granulated sugar in the top layer. This method has been used by many researchers in the past, including McDougall (1979), Hannoun (1985), and Barrett & Van Atta (1991). The combined error of the density readings and the flow meter readings (used to set the free stream velocities) leads to an estimated possible initial Richardson number error of $\pm 7\%$.

2.3. Fluorescence visualization

All flow visualization presented here was accomplished with fluorescein dye and a sheet of light. The light sheet was created with an ordinary slide projector and a slide with a 0.15 mm slit. Fluorescein salt was added and mixed into the entire bottom layer supply before running an experiment. Images were acquired continuously with a video camera.

The camera positioning for side viewing and end viewing are shown in figure 4. Side viewing was used for qualitative flow visualization and for acquiring shear layer growth information. When growth data were desired, a slide with a wide slit was placed in the projector and the light was focused so that one full spanwise period was visible. The point of the wider sheet was to integrate the shear layer thickness through one spanwise wavelength. End views were used to observe the three-dimensional instabilities.

Because we forced the flow temporally at the natural roll-up frequency of the Kelvin–Helmholtz structures, the flow was *nearly* periodic. Thus it was informative to average data based upon the phase of the forcing function, or, in other words, upon the streamwise location within the Kelvin–Helmholtz structures as they passed through a stationary measurement position. This was most useful for reducing velocity data, but in order to correlate the velocity data with the image data, phase-averaging of images was done as well. This was accomplished by strobing the light sheet in phase with the forcing mechanism and continuously acquiring images with the video camera. The images could then be averaged at a later time. These images used for averaging were acquired separately from the continuous video data used for flow visualization.

When using the induced fluorescence technique in this manner, concentrated vorticity can be detected only when it is located near an interface between lower- and upper-layer fluid. Observation of vorticity can become increasingly difficult when the flow is stratified, as motion of a stable interface is then suppressed. Thus, it is important to have some quantitative information about the velocity field in the flow, which was accomplished with laser-Doppler anemometry.

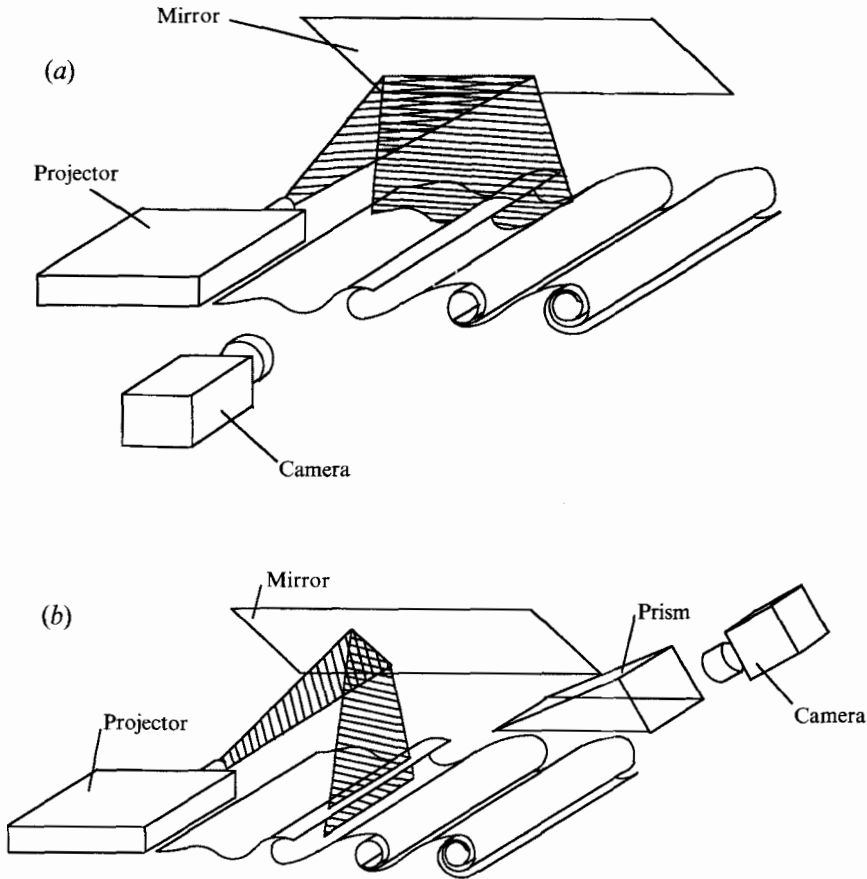


FIGURE 4. Camera and light sheet orientation for (a) side viewing and (b) end viewing. The prism was suspended such that the bottom just touched the free surface of the channel.

2.4. Laser-Doppler measurements

All velocity measurements were made with a laser-Doppler anemometer set up in one-component backscatter mode. A traversing mechanism allowed computer controlled positioning and the raw light intensity data was processed with a burst spectrum analyzer.

Nonlinear terms in the equation for refractive index lead to index variance at the interface between upper- and lower-layer fluid. This can result in a maximum velocity error of about 4.5%. This error, however, is extremely unlikely as it occurs only when a velocity is being measured within the interface (on the order of 10^{-3} cm thick) and is this large only when the interface is at an angle of less than 1° to one of the laser beams.

The data for the mean streamwise velocity profile shown in §2.1 were acquired for 30 s at each station at an average rate of about fifty bursts per s. The laser beams were oriented to measure u , the velocity in the x -direction. In order to get phase-averaged velocity vector plots in the regions surrounding the streamwise vortices, we acquired data at 49 points on a $6 \text{ mm} \times 6 \text{ mm}$ grid for approximately sixty Kelvin-Helmholtz periods. The components measured were v , the velocity in the spanwise y -direction, and w , the velocity in the vertical z -direction. Phase information from the forcing

signal generator was recorded along with the velocity information. Thus, the time of occurrence of each velocity measurement could be related to the phase of the Kelvin–Helmholtz forcing, enabling phase-averaging.

For a more detailed account of all experimental procedures and equipment, see Schowalter (1993).

3. Experimental results and discussion

3.1. Naturally developing three-dimensionality

We begin the description of the experimental results by presenting a visual observation of the natural three-dimensional development of the stratified shear layer at an initial Richardson number of 0.06 and with initial conditions imposed by a straight splitter plate trailing edge. Figure 5 shows fluorescence visualization images of the side view of the shear layer for $0 < x/\theta_0 < 54$ and for $54 < x/\theta_0 < 108$. The lower-layer fluid contained the fluorescein dye. The light sheet was positioned in the center of the span of the shear layer and was about 1 mm thick. The sharp interfaces in the first image reveal the initial two-dimensionality of the shear layer. As we move further downstream, the interface becomes less sharp, indicating small-scale three-dimensionality within the light sheet.

Figure 6 shows visualizations of an end view cut through the centre of the roller core. The upper bright region in (a) is the lower-layer fluid which is entrained by the vortex core and pulled over the top of it. The dark region in the centre is the entrained upper-layer fluid. Some three-dimensionality is visible from this view as there is a noticeable hump in the heavy overturned layer shown by the arrow. After this particular experiment, we observed a small bubble in the tape which secured the splitter plate tip. The bubble was at the same spanwise location as the observed hump. As mentioned by Jimenez (1983), small perturbations in initial conditions can change the position of or enhance streamwise vortices. Thus, it was apparently the perturbation caused by the bubble which gave way to the hump structure. In (b), at $x/\theta_0 = 70$, we see stronger three-dimensionality, especially at the spanwise location of the hump in (a). In addition, we can see three-dimensionality in the layer of entrained lower fluid as it wraps underneath the roller. Clear streamwise vortex structures are visible at $x/\theta_0 = 95$. These vortices appear to be creating the small scales in the flow and they seem to be different in character than streamwise vortices previously observed in homogeneous flows. Streamwise vortices occurring in the homogeneous flows at the top of the roller core form on the upper side of the layer of entrained lower fluid, as that is where the vortex stretching is strongest. Here, we see vortices forming on the lower side of this layer. The image in (d) at $x/\theta_0 = 133$ is shown to demonstrate the fine-scale structure and the evidence of its initiation by the three-dimensional vortex structures. The scalar structure seems to be most complicated in the spanwise regions where three-dimensionality was first observed.

In the experiments that follow, the indented splitter plate was used. In this manner, the structures would grow from a strong single-wave spanwise perturbation.

3.2. Shear layer growth with the three-dimensional perturbation

In order to observe the effect of initial Richardson number on overall shear layer growth with the imposed spanwise and temporal perturbations, the side view light sheet was expanded to contain one full spanwise period. Sixty four video images for each downstream station were digitized, averaged and then processed to obtain

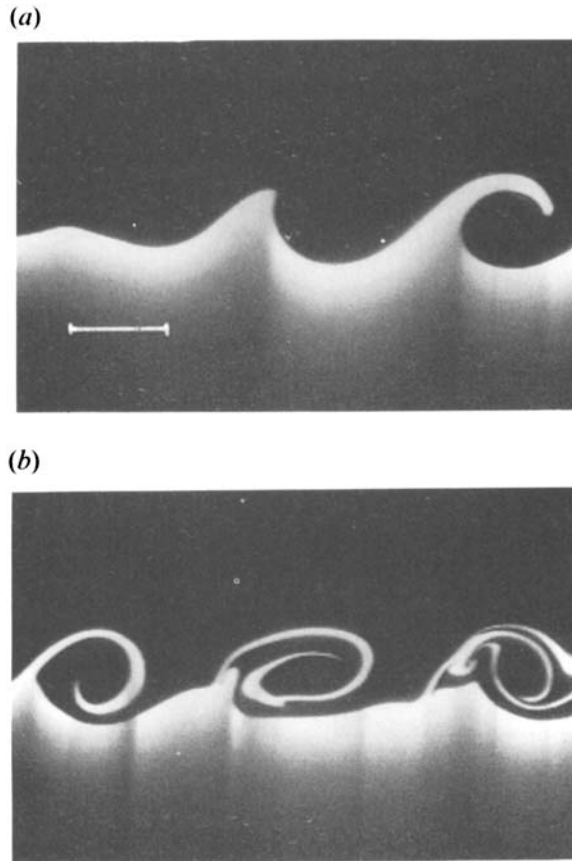


FIGURE 5. Side view of shear layer with flat splitter plate trailing edge, $Ri_0 = 0.06$. (a) $0 < x/\theta_0 < 54$. (b) $54 < x/\theta_0 < 108$. Lengthscale shown in (a) corresponds to 2 cm.

concentration thickness. One of these averaged images is shown in figure 7. Thickness was determined by using a 95% level thickness between the darkest and brightest portions of the image.

Figure 8 contains the results of this processing. The data for $Ri_0 = 0$ are not available as far downstream as for the other cases because the shear layer grew vertically beyond the range of the camera. The initial rapid growth is very similar for all Richardson numbers. The thickness decreases for the stratified cases as the primary Kelvin–Helmholtz mode saturates. Strong streamwise vortices and subharmonic pairing lead to further rapid growth for the unstratified case, while the thickness remains at nearly a constant level after this initial decrease for all of the stratified cases. No pairing was observed for any of the stratified cases, pairing being subdued by the stratification (see Koop & Browand) and by the strong forcing at the fundamental frequency.

The curves for $Ri_0 > 0$ look qualitatively very similar to those shown in Koop & Browand (1979, figure 13). The shear layer grows much more quickly in this case, however, due to the forcing.

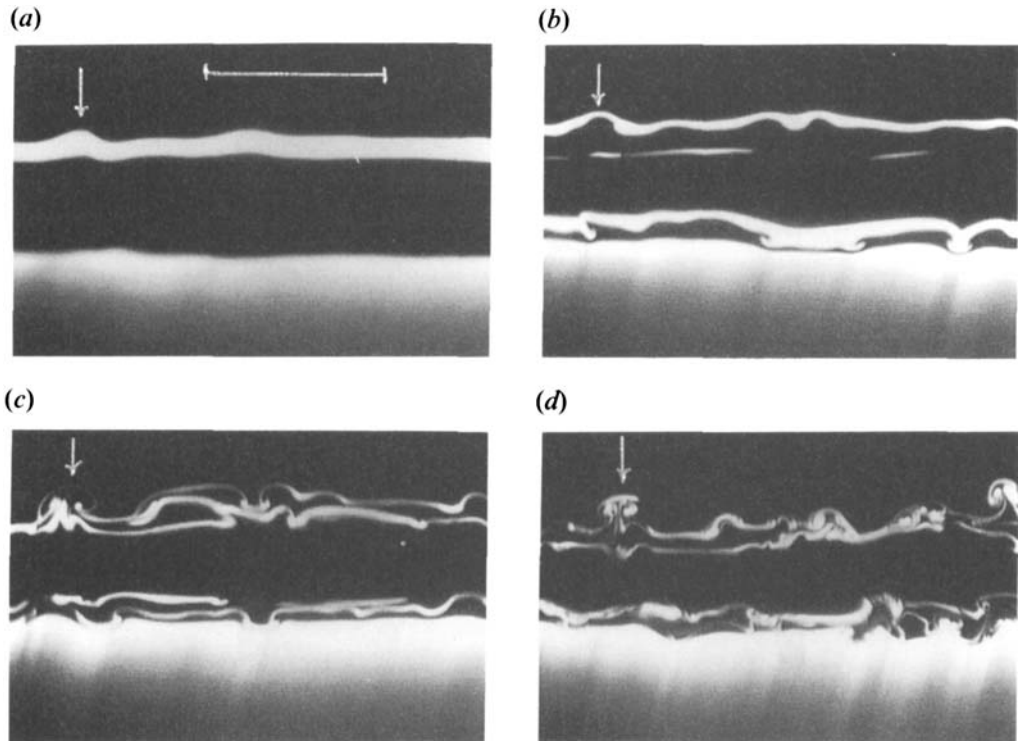


FIGURE 6. End view of shear layer with flat splitter plate trailing edge, $Ri_0 = 0.06$. (a) $x/\theta_0 = 32$. (b) $x/\theta_0 = 70$. (c) $x/\theta_0 = 95$ (d) $x/\theta_0 = 133$. Arrows show spanwise location of small unintentional perturbation caused by bubble in tape on splitter plate. Lengthscale in (a) corresponds to 2 cm.

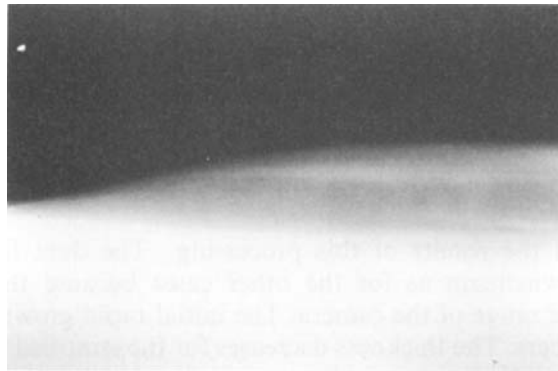


FIGURE 7. Averaged side view image for $Ri_0 = 0$ with indented splitter plate trailing edge, $0 < x/\theta_0 < 54$.

3.3. Visualization and velocity results with the three-dimensional perturbation

The following section is devoted to experimental results with the indented splitter plate tip in place. First, we discuss the effect of stratification on streamwise vortex tubes (also referred to in the literature as ribs).

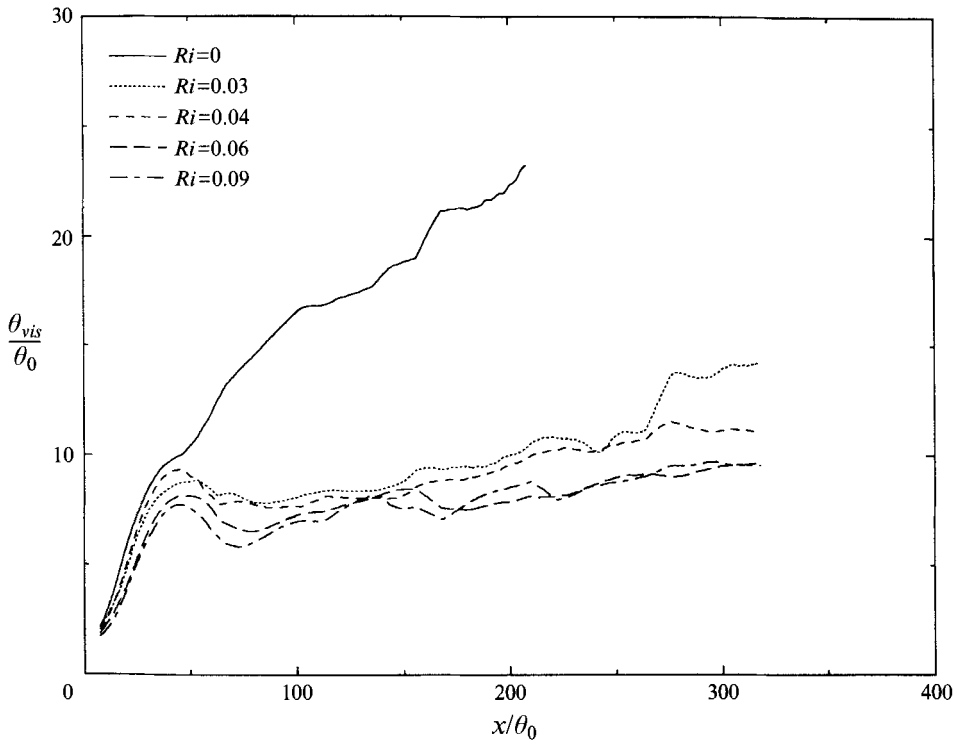


FIGURE 8. Growth of visual thickness with indented splitter plate for various initial Richardson numbers

3.3.1. Streamwise vortex tubes

Figure 9, taken from Lasheras & Choi (1988), shows the vortex tube structure in the homogeneous shear layer. The Kelvin–Helmholtz cores are aligned mainly along the y -direction, and the tubes are represented by the thin curves lying between the cores and wrapping around them. These strong tubes are created by the amplification of perturbations in spanwise vorticity in the ‘braid’ region between the cores. The amplification results from the strong stretching of the strain fields there.

In figure 10, we show the vortex structure with successive end views at $x/\theta_0 = 70$ for the $Ri_0 = 0$ case. The succession begins and ends with the view through the centre of the core and, hence, covers one Kelvin–Helmholtz period. It can be seen clearly that the tubes wrap over the top of one core and underneath another. It is useful to compare the images shown in figure 10 with the schematic drawing in figure 9. The tubes wrapping initially over (underneath) the core forming the upward (downward) mushrooming structure are really part of one continuous hairpin. This hairpin continues to wrap around the core, though its most visible footprint is the mushroom structure. The vorticity is most amplified in the braids and directly above and below the cores, the stretching in these regions being much stronger than within the core. Upon close inspection, however, the hairpins can be observed as they wrap around the core. The hairpin wrapping over the top of the core to the far right in figure 10(a) (shown with the upper arrows) can also be observed at the bottom of the core (shown with the lower arrows). In this region, the bright lower-layer fluid forms a structure that resembles two hooks just touching each other horizontally. This is

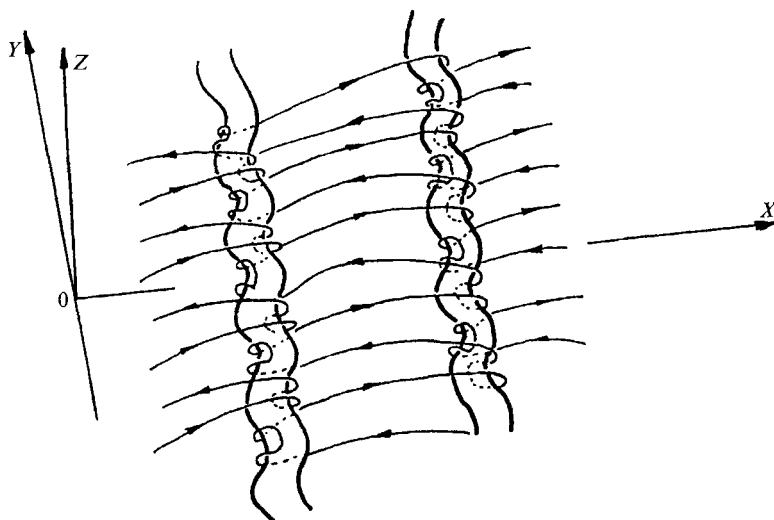


FIGURE 9. Three-dimensional vortex structure for a homogeneous shear layer. Y is the spanwise direction and X is the streamwise direction. From Lasheras & Choi (1988).

not as clear in the other spanwise periods. The influence of the bottom hairpins can also be observed as they wrap around the core. Notice the distortion of the topmost layer of bright fluid in figure 10(*h*) (shown with the upper arrows) directly above the lower downward mushrooming structures (shown with the lower arrows).

To quantify the strength of the vortex tubes in the homogeneous and in the stratified flows, velocity measurements on the grid mentioned in §2.4 were phase-averaged. The forcing period was divided into 32 phases and the velocity at each point was subsequently averaged separately for each phase. Phase-aligned images recorded on video tape were averaged after digitization, enabling a phase-averaged image of the flow. Sixty images were averaged in all cases, corresponding to the roughly 60 periods of velocity data at each point on the grid. Figure 11 shows both the phase-averaged image and vector plot for the $Ri_0 = 0$ case at $x/\theta_0 = 70$ and phase $\phi = 129^\circ$. The phase was chosen to catch the billow near its maximum amplitude. This phase, therefore, corresponds roughly to Figure 10(*a* and *h*). By looking at the averaged image, we can see that the periodicity of the flow is quite striking. It should be stressed, however, that all 60 images which comprise this average were acquired successively. Between different experimental runs, there would be slightly more variation. This is an important point, as the image data and the data for each component of the velocity were taken on separate days. In order to test repeatability, each component of velocity was measured twice (four experiments altogether). The circulation around the entire grid was then calculated using all four possible combinations of the components. The standard deviation was approximately 11% of the mean circulation, indicating acceptable repeatability of tube circulation. The mean circulation, non-dimensionalized by the Kelvin–Helmholtz circulation ($\Gamma_{KH} = \lambda_{KH}\Delta U$) was -8.2×10^{-2} . So the spanwise perturbation has given way to streamwise vortices containing roughly one tenth of the overall circulation for one spanwise period. The next step is to see how stable stratification affects these structures.

Successive video images at $x/\theta_0 = 70$ with $Ri_0 = 0.06$ are shown in figure 12. The streamwise vortex tubes are visible in the spanwise period at the centre of the

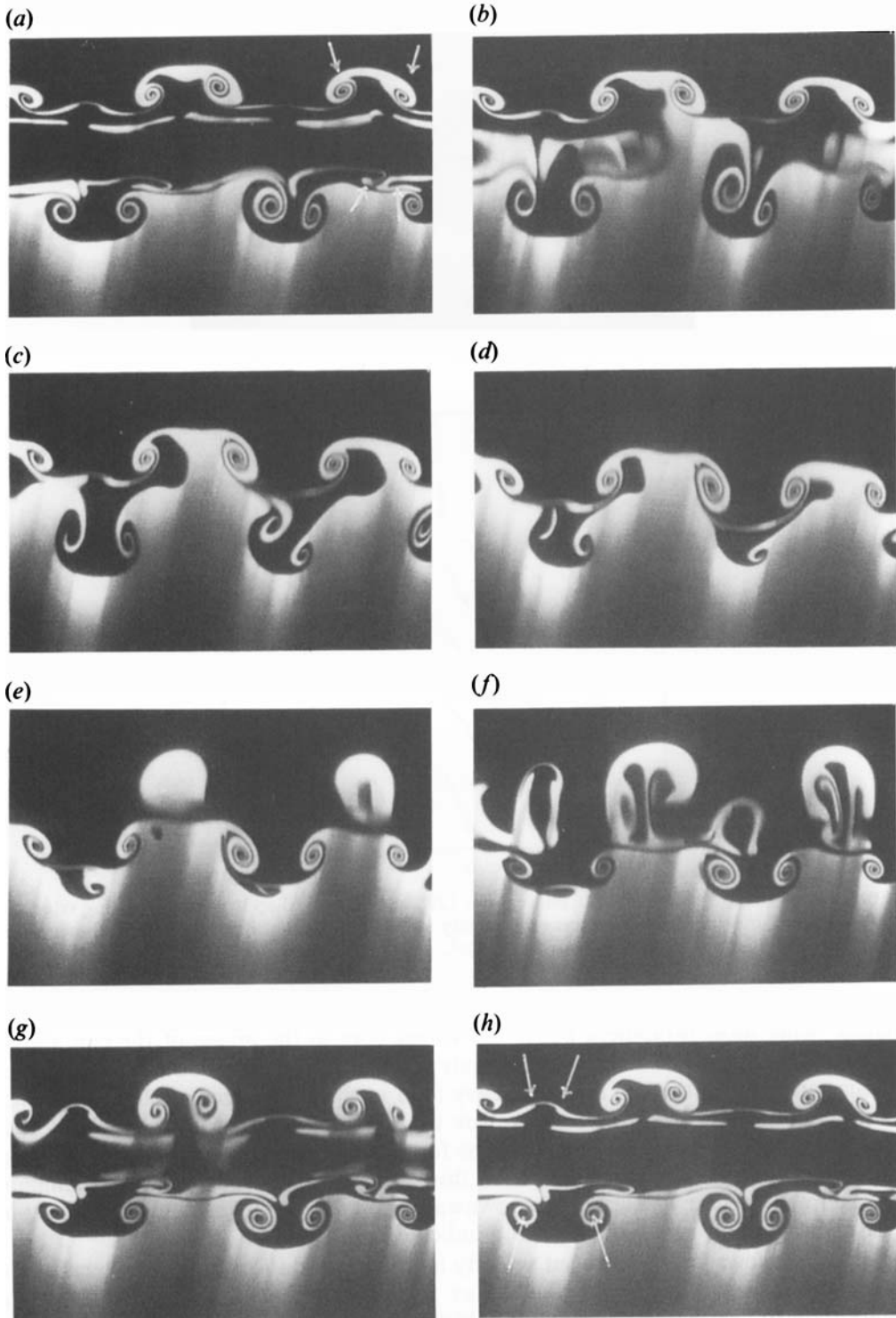


FIGURE 10. Successive end view fluorescence images for $Ri_0 = 0$ with indented splitter plate trailing edge, $x/\theta_0 = 70$. Time increases from (a) to (h). Arrows in (a) and (h) show locations of hairpin vortices. Time between images is 0.067 s.

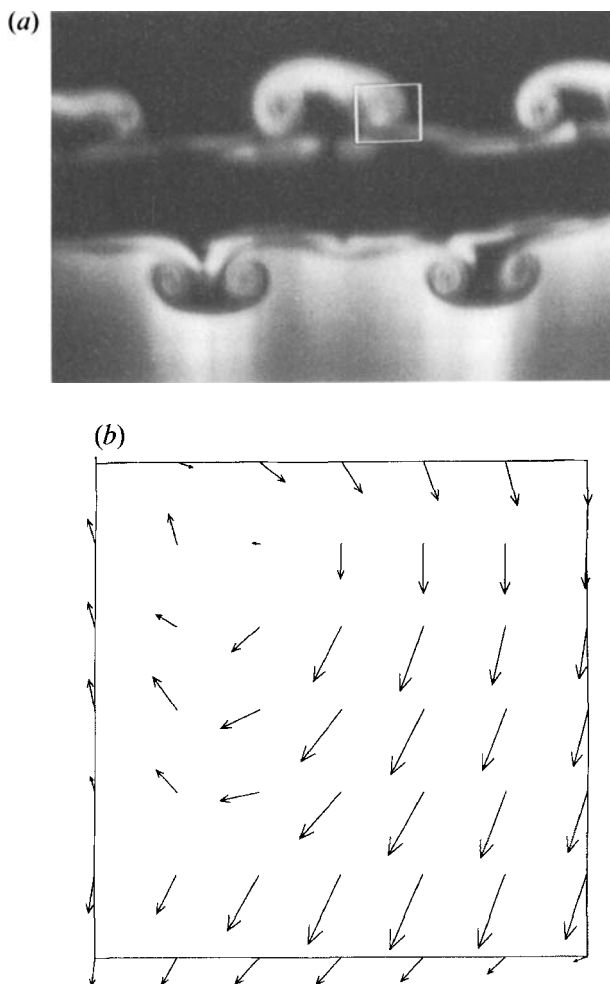


FIGURE 11. $Ri_0 = 0$, $x/\theta_0 = 70$, and phase, $\phi = 129^\circ$ with indented splitter plate trailing edge. (a) Phase-averaged image. (b) Phase-averaged velocity within highlighted box in (a). Non-dimensional circulation of entire grid is $\Gamma/\Gamma_{KH} = -8.2 \times 10^{-2}$.

images, being most prominent above the vortex core in the image of the core cross-section. They appear to have been severely weakened, although we can see vortices forming underneath the top layer of heavy fluid in the core directly below the vortex tubes. Arrows indicate one of the vortex tubes (from the hairpin) and the vortex forming below this heavy layer in (a). The footprint of the upper tubes as they wrap underneath the core are much clearer in this case than in the $Ri_0 = 0$ case (compare with figure 10). Here we clearly see downwardly mushrooming structures in the thin layer of heavy fluid below the core and indicated in (b).

Figure 13 shows phase-averaged velocity and image data for this case. To calculate the circulation associated with the vortex for this stratification, it does not seem appropriate to use the entire region in which velocity measurements were made. The vortex in the image appears to occupy a smaller area than in the unstratified case. In addition, it would be undesirable to include the vorticity which has formed on the lower interface, since it does not appear to be associated with the tube structure.

Thus, a smaller circuit has been chosen to calculate the circulation. Although the circuit may seem rather arbitrary, the choice is based upon the position of the dye in the visual image. This method of choosing a circuit is used throughout the remainder of this paper. In §3.5, we show that, although some of the vorticity associated with the structure in question may be eliminated by this choice of integration path, most of it is included and the associated error is small enough to determine trends associated with the development of the vortices being observed.

The laser-Doppler measurements in figure 13 confirm the apparent visual observation of the stratification-induced weakening of the upper vortex tube. In addition, the vortex forming at the base of the thin upper layer of heavy fluid can be observed. This vortex will be addressed in §3.3.2. Looking at the vector plot, there does not appear to be a clear vortex in the region where the tube is visible in the image.

Calculating the circulation around the dashed region, we get a result of $\Gamma/\Gamma_{KH} = 1.5 \times 10^{-2}$. This circulation is not only smaller than that calculated in figure 11 (-8.2×10^{-2}) but is *positive* as opposed to negative.

The next question to address experimentally is how does the strength of the initially upper vortex tube change as it wraps underneath the core. Figure 14 tracks the vortex tubes as they wrap around the core at $x/\theta_0 = 83$. The arrows show the location of the tubes within the plane. Time moves backward from (a) to (f), but it may be more illustrative to think of the vortex core as being stationary and of the light sheet as moving downstream through it. The upper and lower portions of the tubes can be seen to connect in (f), at the downstream edge of the core. So we see that, for this particular spanwise period, there is a rather complicated positioning of the wrapping portion of the tubes. One lies above the other, rather than both lying side by side. To show the vortex strength in this region, phase-averages for $Ri_0 = 0$ at $x/\theta_0 = 83$ are shown in figure 15. The dashed region surrounding the vortex tube has the small positive circulation of 0.25×10^{-2} . It seems curious that this circulation is so much smaller than the value of -8.2×10^{-2} that we calculated for this vortex tube at a position above the core (note the sign changes due to the wrapping of the vortex filaments around the spanwise core). The strongest stretching of the vortex filaments occurs in the braid region, however, so the vorticity will be much more diffuse within the core. In fact, some of the vortex filaments contained in the tube may not be pulled around below the core, giving a smaller circulation in that region. In the numerical simulation of Rogers & Moser, the vortex lines connecting the tubes remained above the core due to the mutual induction caused by the hairpin shape. We do, however, notice evidence of some vorticity being wrapped around the spanwise core.

The effect of stratification on this part of the vortex tube is clearly visible in figure 16. In (a), there is a clear downwardly mushrooming structure, half of which is in the highlighted box. The circulation of the vortex tube within the box is 4.6×10^{-2} as compared with the strength of the corresponding vortex for $Ri_0 = 0$ of 0.25×10^{-2} . Thus, the vortex tubes are strengthened in these regions of static instability, whereas we have seen that they are weakened in regions of static stability. This can be explained through inspection of the baroclinic torque in these regions. The inviscid vorticity transport equation for a stratified fluid is

$$\frac{D\boldsymbol{\omega}}{Dt} = \boldsymbol{\omega} \cdot \nabla \mathbf{u} + \frac{1}{\rho^2} (\nabla \rho \times \nabla p), \quad (3.1)$$

where $\boldsymbol{\omega}$ is the vorticity vector, \mathbf{u} the velocity vector, ρ the density, and p the pressure. The baroclinic torque is the cross-product on the right-hand side of the equation. Although there is density variation in this equation, the flow is considered

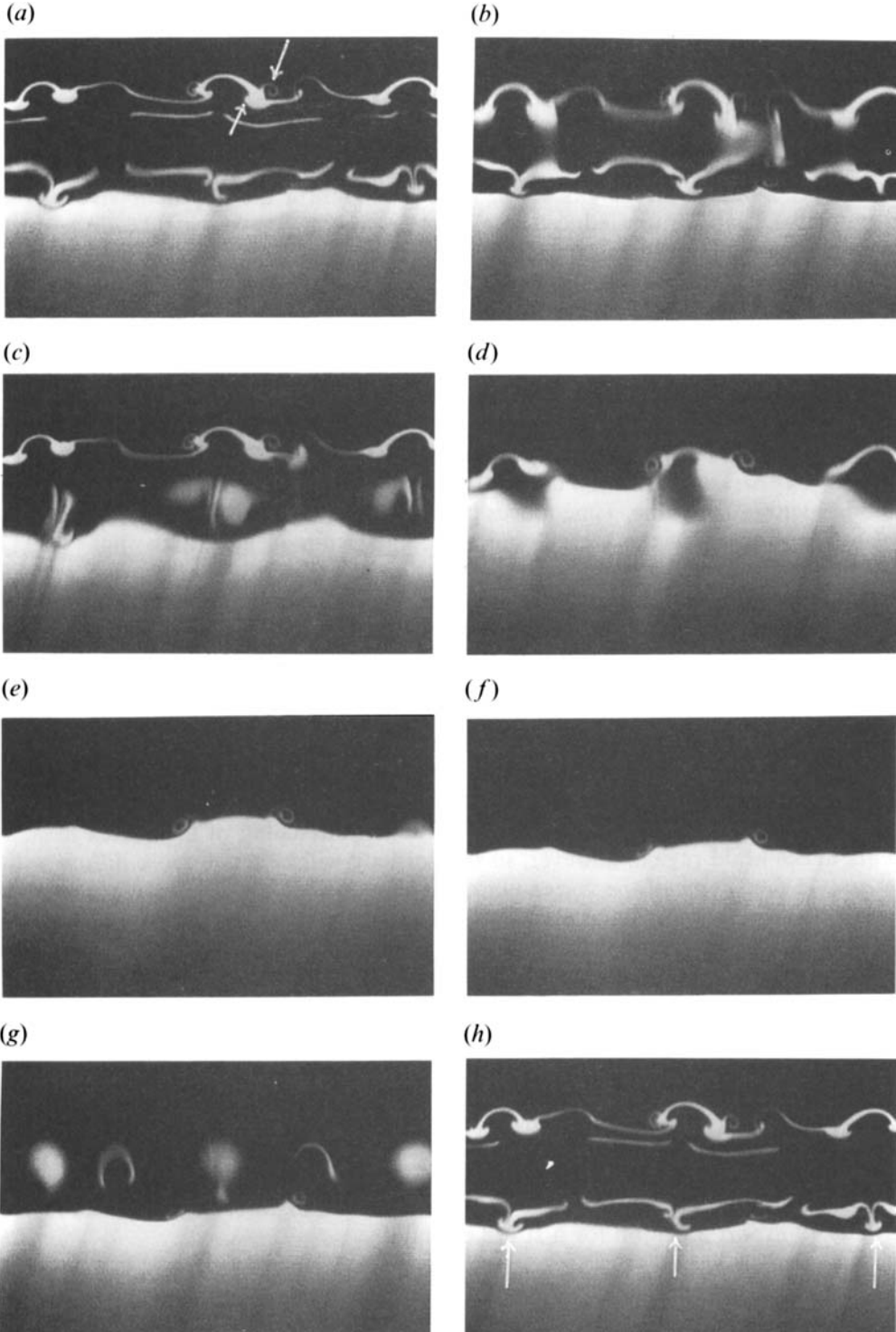


FIGURE 12. For caption see facing page.

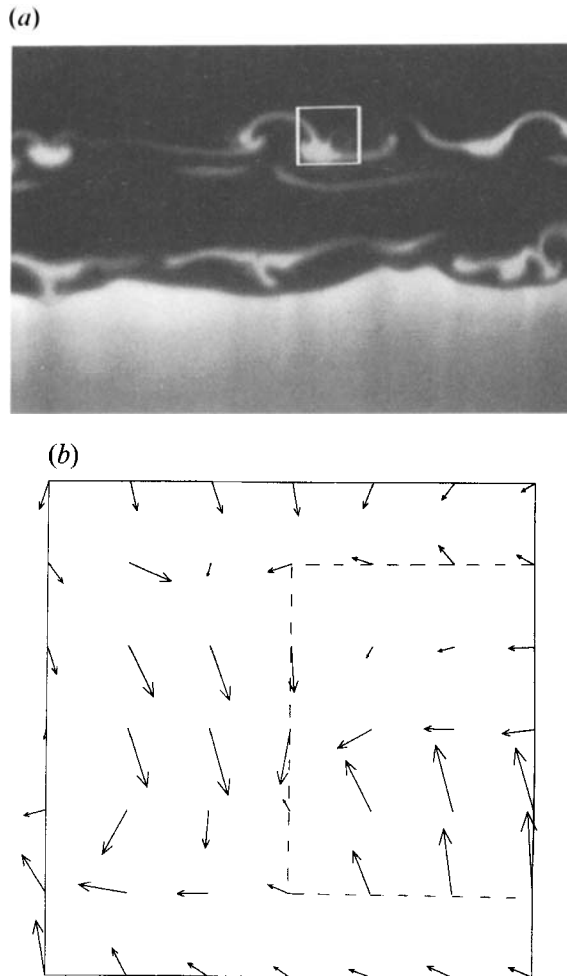


FIGURE 13. $Ri_0 = 0.06$, $x/\theta_0 = 70$, and phase, $\phi = 118^\circ$ with indented splitter plate trailing edge. (a) Phase-averaged image. (b) Phase-averaged velocity within highlighted box in (a). Non-dimensional circulation of dashed region is $\Gamma/\Gamma_{KH} = 1.5 \times 10^{-2}$.

incompressible. Inviscidly, the pressure gradient can be expressed as

$$\nabla p = -\rho \frac{Du}{Dt} + \rho g \approx \rho g. \quad (3.2)$$

The inertial component of the pressure gradient turns out to be less than four per cent of the hydrostatic portion when the Kelvin–Helmholtz roller is modelled as a Stuart vortex. Thus, ∇p will always be directed downwards. Consider figure 17, a cartoon for the behaviour of the layers in the cross-section of a Kelvin–Helmholtz roller. The

FIGURE 12. Successive end view fluorescence images for $Ri_0 = 0.06$ with indented splitter plate trailing edge, $x/\theta_0 = 70$. Time increases from (a) to (h). Arrows in (a) show the vortex tube structure as well as the vortex forming below the heavy overturned layer. Arrows in (h) show downward mushrooming structures where vortex tubes wrap around core. Time between images is 0.067 s.

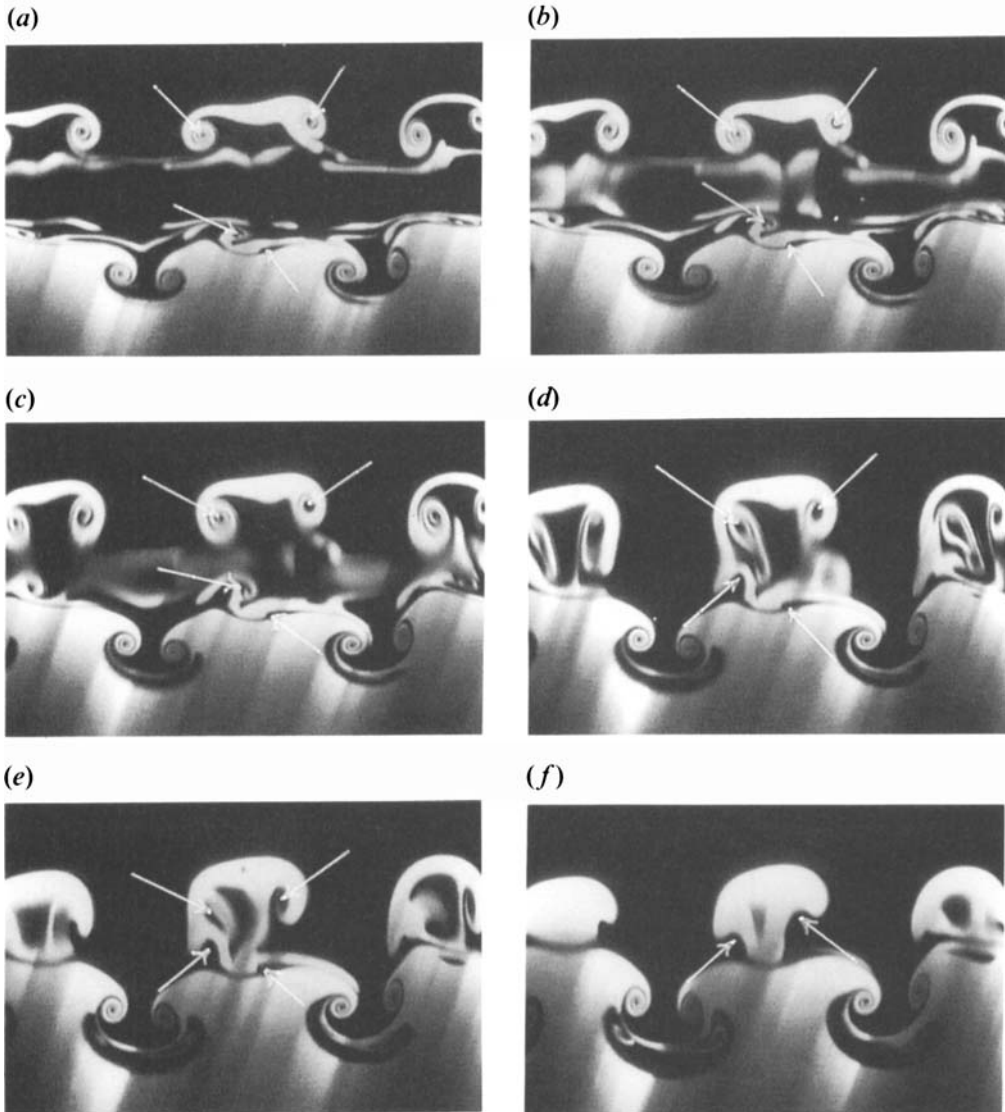


FIGURE 14. Time evolution of wrapping vortex tube position for $Ri_0 = 0$, $x/\theta_0 = 83$ with indented splitter plate trailing edge. Time moves negatively from (a) to (f) with a separation between frames of 0.033 s. Conceptually, it may be best for the reader to consider this a spatial evolution in which the light sheet begins at the position of maximum billow amplitude and moves forward.

tubes can be seen wrapping over the top of the roller and underneath the roller. The layers are perturbed by the tube structures, creating a non-zero baroclinic torque. In statically stable regions, the baroclinic torque has the opposite sign of the local tube structure, weakening the tubes. In statically unstable regions, however, the baroclinic torque has the same sign as the local vortex, and the tubes are strengthened.

3.3.2. Baroclinically generated streamwise vortices

We now focus our attention on the streamwise vortices which form below the top layer of heavy fluid which is pulled over the Kelvin–Helmholtz spanwise roller

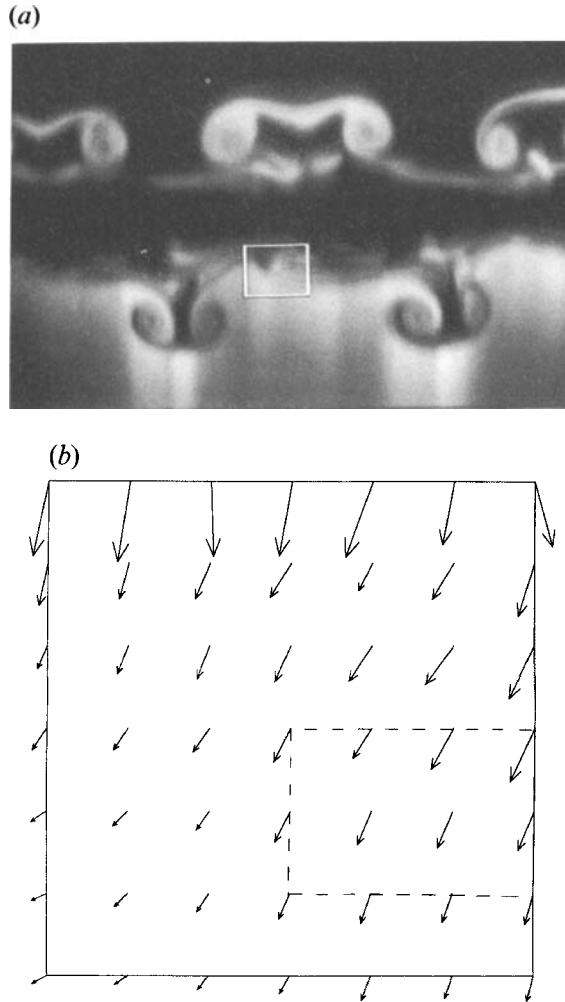


FIGURE 15. $Ri_0 = 0$, $x/\theta_0 = 83$, and phase, $\phi = 17^\circ$ with indented splitter plate trailing edge. (a) Phase-averaged image. (b) Phase-averaged velocity within highlighted box in (a). Non-dimensional circulation of dashed region is $\Gamma/\Gamma_{KH} = 0.25 \times 10^{-2}$.

core. These are observed only in the non-zero Richardson number case and can be distinguished from the vortex tubes in that the tubes form at the top of this heavy fluid layer. This is the instability which Klaassen & Peltier named ‘convective roll’ due to its relationship to the Rayleigh–Taylor instability.

Figure 18 is similar to figure 13(b), but the circulation is now calculated around the region enclosing the vortex at the unstable interface. The initial Richardson number is 0.06 and x/θ_0 is 70. The heavy fluid can be seen ‘draining’ downwards in the middle left of the vector plot, whereas the light fluid can be seen moving upwards in the lower left of the plot, this convective motion being associated with baroclinic generation of vorticity. The dimensionless circulation inside the dashed region is calculated to be $\Gamma/\Gamma_{KH} = -1.2 \times 10^{-2}$, not yet very significant when compared to the vortex tube in the $Ri_0 = 0$ case, but similar in strength to the vortex tube for this flow, whose sign has been reversed by the baroclinic torque, as discussed in § 3.3.1.

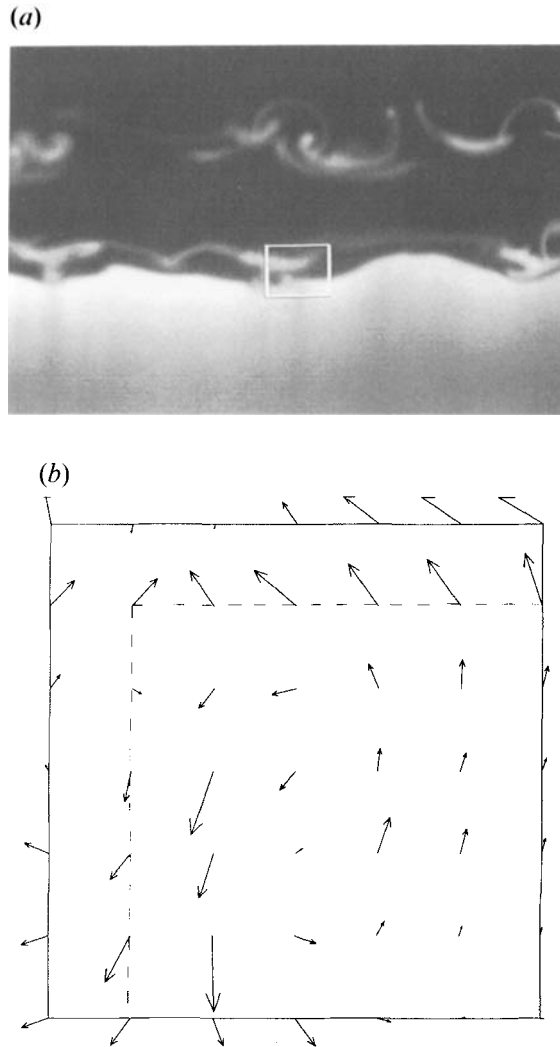


FIGURE 16. $Ri_{0.06} = 0$, $x/\theta_0 = 83$, and phase, $\phi = 28^\circ$ with indented splitter plate trailing edge. (a) Phase-averaged image. (b) Phase-averaged velocity within highlighted box in (a). Non-dimensional circulation of dashed region is $\Gamma/\Gamma_{KH} = 4.6 \times 10^{-2}$.

Figure 19 shows how this vortex has developed at $x/\theta_0 = 83$. The phase-averaged image shows the vortex very clearly in the centre of the highlighted box and the vector plot suggests a vortical structure as well. In this case, the dimensionless circulation over the dashed region is $\Gamma/\Gamma_{KH} = -3.5 \times 10^{-2}$, nearly half the strength of the vortex tube for the unstratified case and a dominant feature at this initial Richardson number. Thus, for $Ri_0 = 0.06$, the buoyancy-generated vortex strength increases downstream between the two measurement stations.

Inspection of the sign of baroclinic torque clarifies the mechanism for the formation of these vortices. Figure 20 again shows the alternating layers of high- and low-density fluid perturbed by the streamwise vortex tubes. Careful examination of the region where the buoyancy-induced vortices form shows that the baroclinic torque will form two vortex sheets of opposite sign along the unstable interface. Each vortex sheet

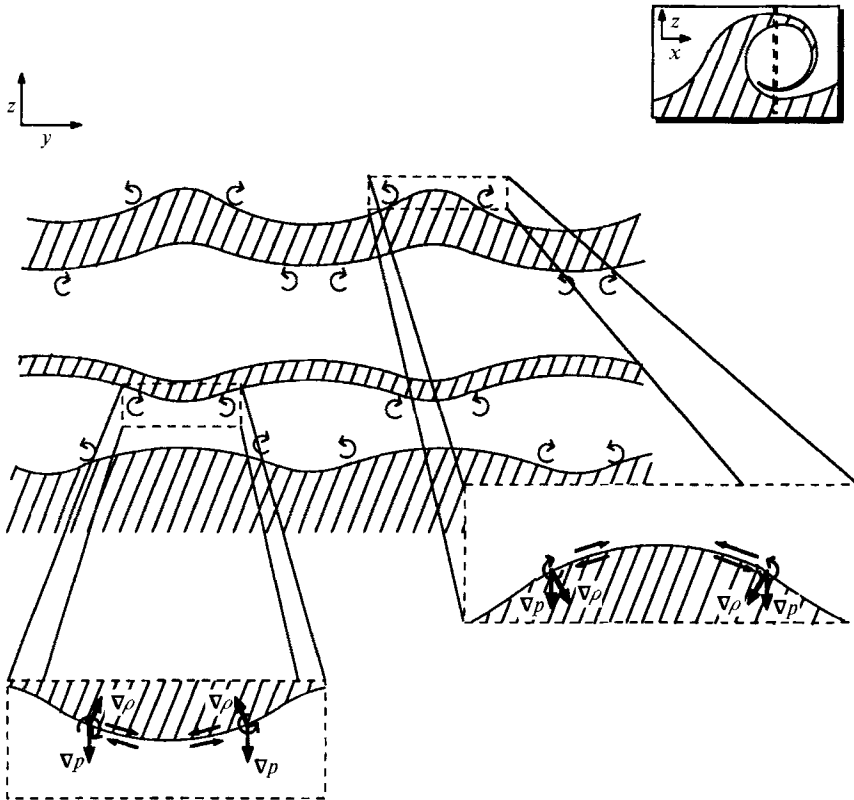


FIGURE 17. Conceptual drawing showing the effect of baroclinic torque on streamwise vortex tubes. They are weakened where there is locally stable stratification and strengthened where there is locally unstable stratification.

will cause a tilting of the other which will lead to a greater cross-product of the pressure gradient and the density gradient, leading to a stronger torque, further tilting, and so on. The rapid growth of vorticity in these sheets eventually leads to a local roll-up, which is the observed buoyancy-induced vortex. In other words, one can consider this instability or the Rayleigh–Taylor instability as being driven by the baroclinic torque and one may refer to these vortices as being baroclinically generated. The streamwise vortex tubes, though eventually severely weakened by buoyancy, provide the initial perturbation for the formation of the baroclinically generated vortices.

Detailed phase-average measurements were made for one other initial Richardson number, 0.09, to obtain at least some quantitative information on the effect of Richardson number on the baroclinically generated vortex development. Figure 21 shows the phase-averaged image and vector plot for $Ri_0 = 0.09$ at $x/\theta_0 = 70$. Although there is no clear roll-up at this phase, vorticity can be seen clearly in the vector plot, where there is strong upward flow of light fluid on the left side. The dimensionless circulation around the dashed region is -3.4×10^{-2} , considerably larger than the strength of the $Ri_0 = 0.06$ vortex at the same downstream position. Figure 22 shows the vortex further downstream, at $x/\theta_0 = 83$. Here, the structure can be observed in the image, but only vaguely in the vector plot. The circulation in this case is only -1.4×10^{-2} , less than the strength further upstream.

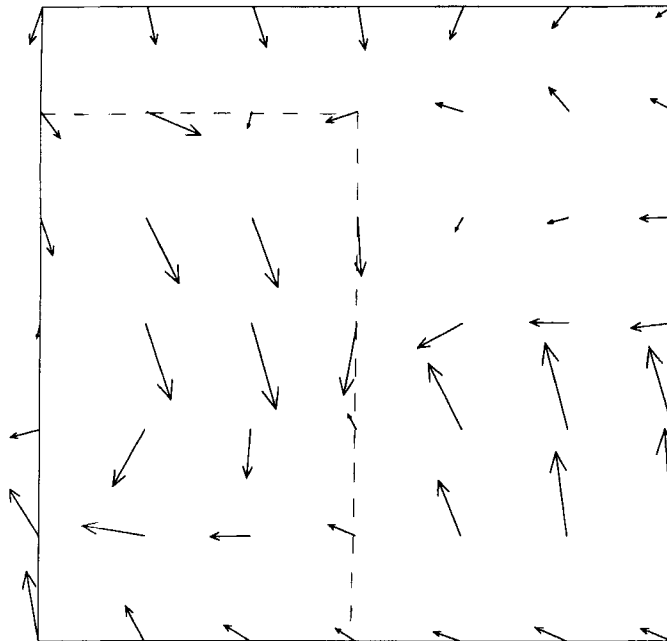


FIGURE 18. $Ri_0 = 0.06$, $x/\theta_0 = 70$, and phase, $\phi = 118^\circ$ with indented splitter plate trailing edge. Phase-averaged velocity within highlighted box in figure 13(a). Non-dimensional circulation of dashed region is $\Gamma/\Gamma_{KH} = -1.2 \times 10^{-2}$.

Figure 23 shows graphically the strength evolution of the baroclinically generated vortices for the two Richardson numbers investigated. Here we observe that, for $Ri_0 = 0.06$, the vortex strength starts small, increasing with downstream distance, whereas for $Ri_0 = 0.09$, the opposite occurs. It is expected that the vortices are initially stronger for larger Richardson numbers because, in that case, the density gradient is larger and, hence, the baroclinic torque is stronger. The mechanism for the weakening of the vortex downstream for the higher Richardson number remains unclear. This will be clarified, however, in §4.2.

During the acquisition of the data presented in §3.2, end views were also recorded on video tape. It was thus possible to observe the approximate downstream distance at which baroclinically generated vortices visually dominate the three-dimensional structure for a variety of initial Richardson numbers. These values are shown in figure 24, with the downstream distance non-dimensionalized by the Kelvin–Helmholtz wavelength. Note that, even for the small initial Richardson number of 0.03, buoyancy-induced vortices eventually become the most important feature of the streamwise vorticity field.

3.3.3. Stretched baroclinic vortices

We now turn our attention to another newly observed three-dimensional structure found in these experiments. Figure 25 shows a top view of the shear layer. The image was acquired during a preliminary qualitative experiment in which the Richardson number was 0.06. In this case, the dye was fluoresced with a spotlight positioned on the side of the channel. The flow is moving from left to right and the spanwise cores can be observed clearly, arranged vertically on the page. The small spanwise-periodic peaks at the downstream edges of the cores are the baroclinically generated vortex

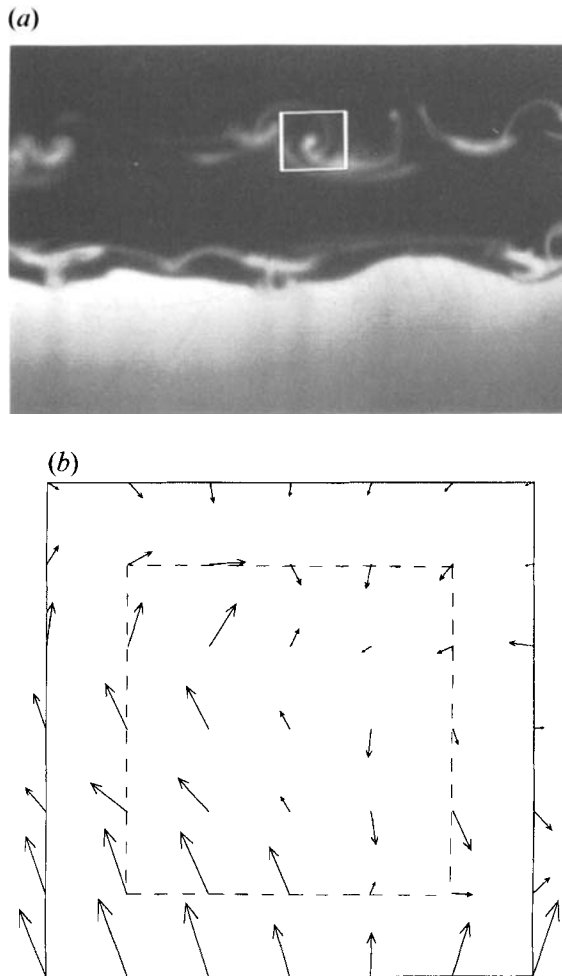


FIGURE 19. $Ri_0 = 0.06$, $x/\theta_0 = 83$, and phase, $\phi = 28^\circ$ with indented splitter plate trailing edge. (a) Phase-averaged image. (b) Phase-averaged velocity within highlighted box in (a). Non-dimensional circulation of dashed region is $\Gamma/\Gamma_{KH} = -3.5 \times 10^{-2}$.

pairs. An additional spanwise sinuous structure, highlighted with a dashed curve, can be observed within the cores. It begins at the upstream edge of the cores, and its spatial amplitude grows downstream, alternate peaks being pulled towards the downstream edge of the core.

These structures can also be clearly seen in end views and here appear to have some vorticity associated with them. Figure 26 shows a frame by frame sequence for $Ri_0 = 0.09$ at $x/\theta_0 = 83$. Time moves forward through the sequence as the spanwise rollers move through the light sheet. The structures in question are first visible in (b), just below the thin top layer of heavy fluid and shown with arrows. They appear as thick, bright horizontal segments. In (c), it is clear that there are vortices with strong streamwise components, and, in (d), it can be seen that the vortices move away from each other, pairing with the baroclinically generated vortices as the upstream edge of the core is approached. It is consistent to interpret the sinuous structure in figure 25 as a vortex filament, which, when cut with a spanwise vertical plane, yields the observed vortex pairs. Two end view sequential images at $x/\theta_0 = 95$ are shown

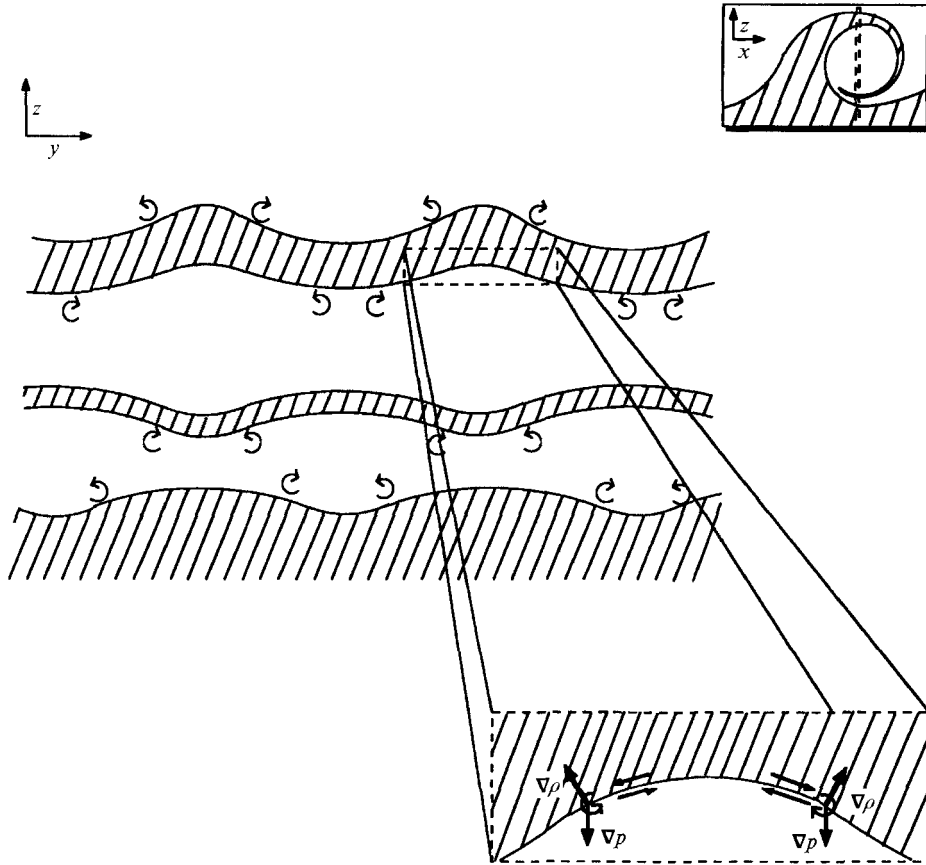


FIGURE 20. Conceptual drawing showing mechanism responsible for buoyancy-generated vortices. The vortex tubes distort the unstable interface causing a non-zero vector product of the pressure gradient and the density gradient.

in figure 27. At this location, we observe not only the pairing with the baroclinically generated streamwise vortices, but the domination of the three-dimensional structure by this new vortex. The question that arises is where is this vorticity created?

Figure 28 shows a side view of the same flow. The light sheet in this case was placed in the spanwise region in which the vortex filament is pulled over the core. The flow is moving from left to right. In the spanwise roller to the left, there appears to be a vortex forming where the thin wisp of heavy fluid attaches to the bulk of bottom-layer fluid. This vortex has the opposite sign to that of the spanwise roller. The existence and sign of this vortex are to be expected, given the baroclinic torque on that interface, as shown in figure 29. In the central spanwise roller in figure 28, this vortex has developed further and has been pushed upward, carrying with it a significant amount of heavy fluid. The vortex has been advected over the top of the roller to the right. Because the vortex filament remains at the upstream edge of the core in some regions, but is pulled over in others, a considerable amount of stretching occurs, leading to further amplification. So this vortex is formed by spanwise baroclinic generation, then stretched by wrapping around the core, pairing in some regions with the streamwise baroclinically generated vortices. Precisely why

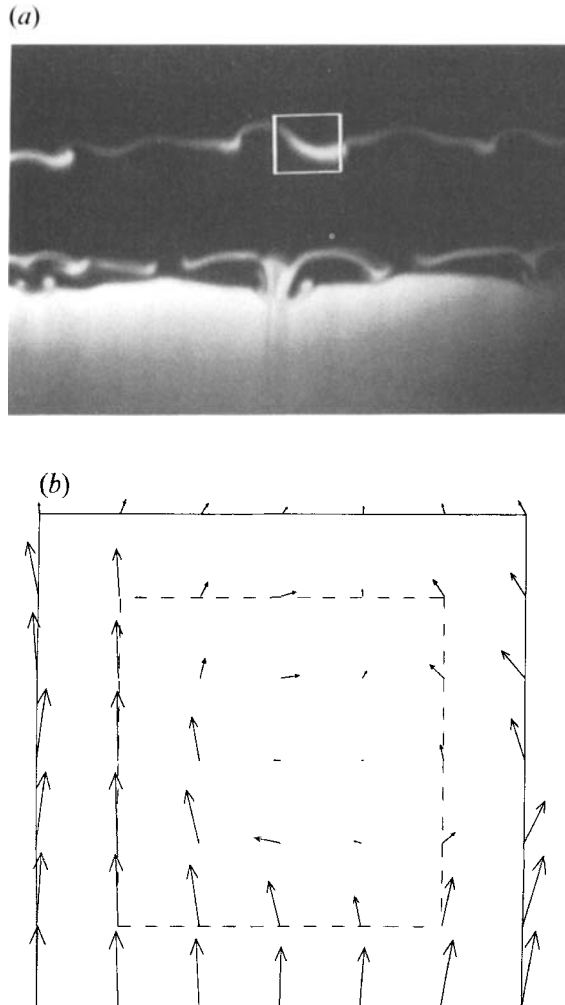


FIGURE 21. $Ri_0 = 0.09$, $x/\theta_0 = 70$, and phase, $\phi = 118^\circ$ with indented splitter plate trailing edge. (a) Phase-averaged image. (b) Phase-averaged velocity within highlighted box in (a). Non-dimensional circulation of dashed region is $\Gamma/\Gamma_{KH} = -3.4 \times 10^{-2}$.

this stretched baroclinic vortex is advected over the core in some regions while not in others is unclear to us.

3.4. Potential energy evolution

To determine the importance of baroclinically generated, enhanced, and weakened vortex structures to the overall flow, average potential energy was calculated at various positions downstream for flows with and without the imposed spanwise perturbation. The initial Richardson number for both cases was 0.06 and calculations were made using end view images. Owing to the rather large Schmidt number (≈ 1500) across the interface separating the two layers, it was assumed that there was no diffusion of mass. Thus, a simple thresholding algorithm was used to determine the portions of the image containing lower-layer fluid and upper-layer fluid. We define average

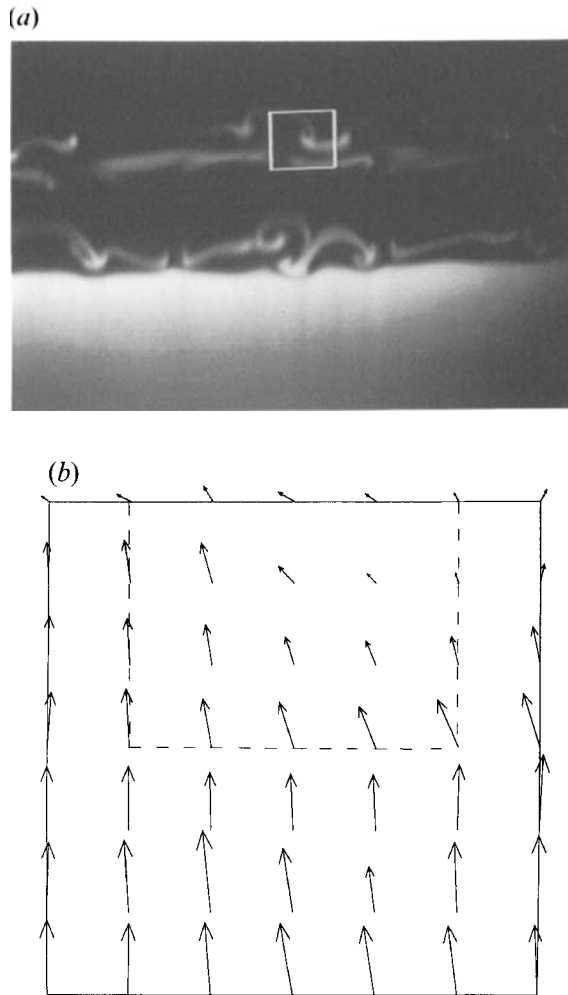


FIGURE 22. $Ri_0 = 0.09$, $x/\theta_0 = 83$, and phase, $\phi = 28^\circ$ with indented splitter plate trailing edge. (a) Phase-averaged image. (b) Phase-averaged velocity within highlighted box in (a). Non-dimensional circulation of dashed region is $\Gamma/\Gamma_{KH} = -1.4 \times 10^{-2}$.

potential energy per unit mass as

$$\bar{\Phi} = \frac{\int_0^T \int_0^L \int_{-\infty}^{\infty} (\rho - \rho_0)gzdzdydt}{T(L\bar{\rho}\delta_{th})} \tag{3.3}$$

where

$$\rho_0 = \begin{cases} \rho_1 & \text{if } z > 0 \\ \rho_2 & \text{if } z < 0 \end{cases} \tag{3.4}$$

The integrand in (3.3) is the work required to move a fluid parcel in the image to its position, T then being the temporal period of averaging, about three forcing periods in our case. The portion of the denominator in parentheses is the mass of fluid in the shear layer in the image. δ_{th} represents the maximum visual thickness of the shear layer at the downstream location in question and was calculated after thresholding. The time integral is estimated by summing over images and the area

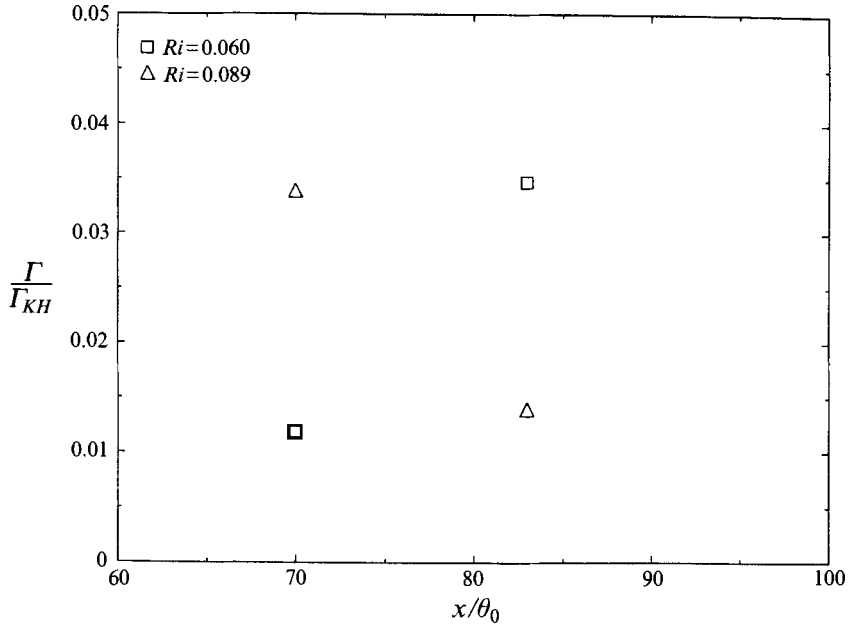


FIGURE 23. Strength evolution of circulation of baroclinically generated vortices.

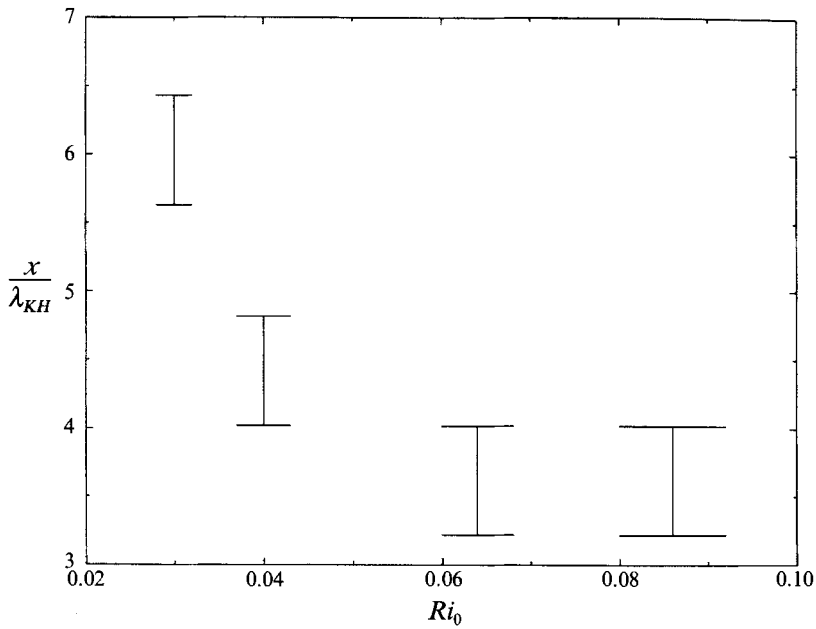


FIGURE 24. Downstream distance at which baroclinically generated streamwise vortices become dominant over vortex tubes enhanced by stretching.

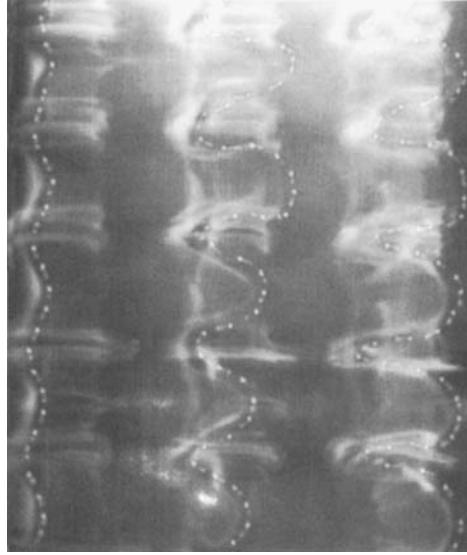


FIGURE 25. Top view of shear layer with indented splitter plate trailing edge showing stretched baroclinic vortices. $Ri_0 = 0.06$.

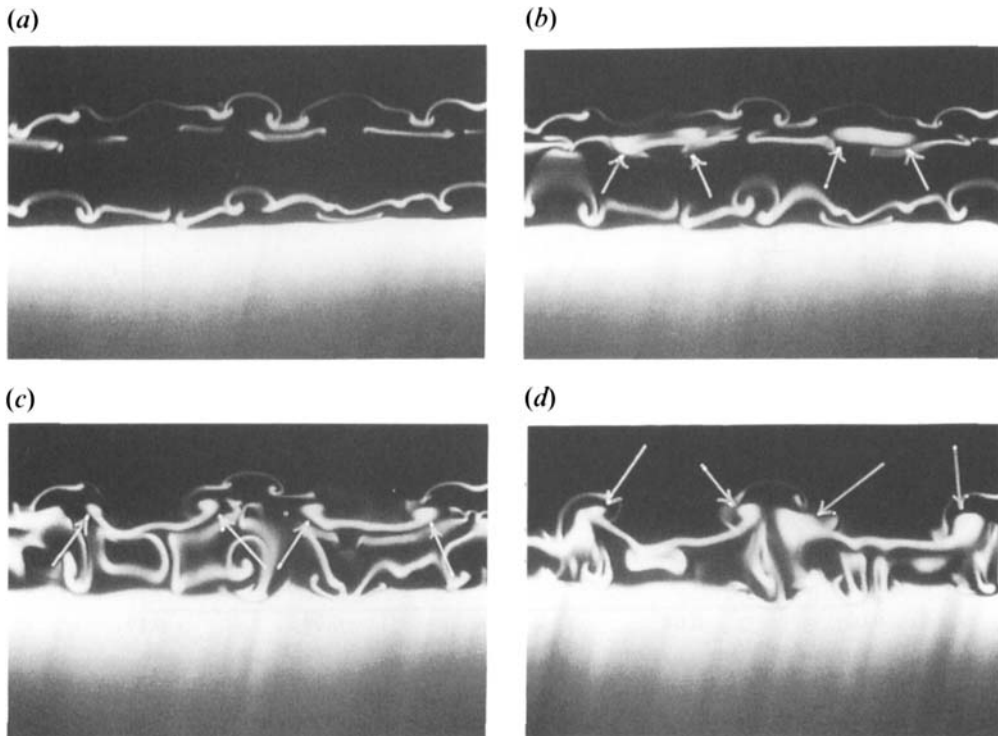


FIGURE 26. Sequential images for $Ri_0 = 0.09$ at $x/\theta_0 = 83$ with indented splitter plate trailing edge. Time increases from (a) to (d) with 0.033 s between frames.

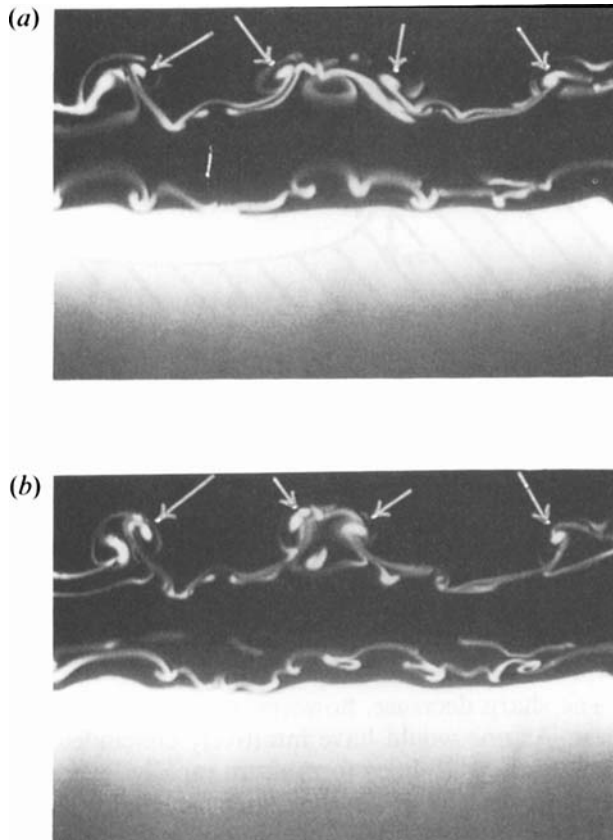


FIGURE 27. Sequential images for $Ri_0 = 0.09$ at $x/\theta_0 = 95$ with indented splitter plate trailing edge. Time increases from (a) to (b). Arrows show positions of vortices.

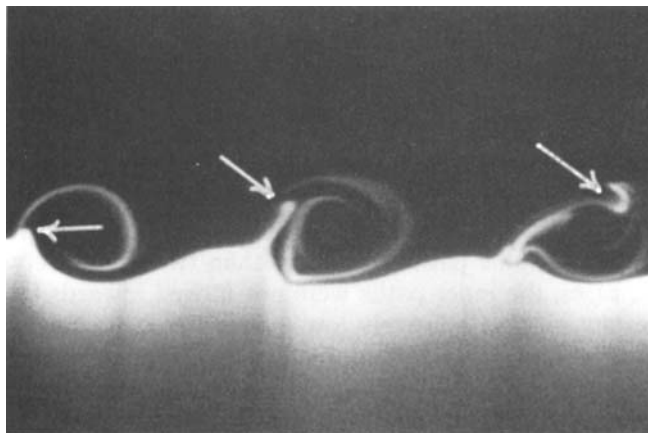


FIGURE 28. Side view of shear layer with indented splitter plate trailing edge. $Ri_0 = 0.09$, $54 < x/\theta_0 < 108$. Light sheet was placed at the spanwise location at which the vortex filament is pulled over the roller.

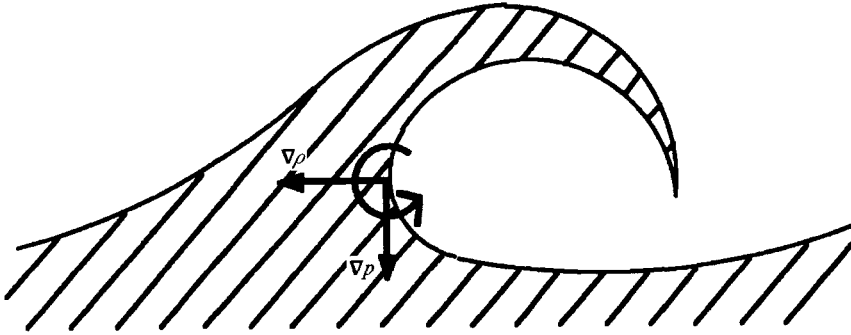


FIGURE 29. Generation of opposite-sign spanwise vorticity concentration by baroclinic torque.

integral by summing over pixels in each image. L , the spanwise extent of integration, corresponded to roughly two spanwise periods in the three-dimensionally perturbed case.

Results are shown in figure 30. It appears that less potential energy is initially created when the indented splitter plate trailing edge is used. This can be confirmed by comparing the amounts of overturned fluid in figures 6 and 12. As this is only an order of magnitude measurement, however, it is most important to compare the general trends of the two curves. As one moves downstream, the potential energy rises then drops sharply in both cases, the rise being due to the increasing amounts of overturned fluid. The sharp decrease, however, occurs further downstream for the spanwise unforced case. As one would have intuitively concluded, the forced case, in which the three-dimensional instabilities form more rapidly, releases potential energy due to overturning more quickly. It seems, then, that the streamwise structures formed and influenced by buoyancy are important in the conversion of potential energy into kinetic energy in the shear layer.

3.5. Circulation error estimates and their relevance to experimental findings

It is appropriate at this point to discuss in detail the error associated with circulation calculation. Although the paths used to calculate circulation were determined based upon the fluorescence images acquired by video, we are not assured that all of the relevant vorticity is included within these paths. To estimate the error resulting from this choice of paths, we employed the following method: for each vector field for which the calculation was made, one larger path was chosen by moving the path one node outward and one smaller path was chosen by moving the path one node inward. In this manner the error could be estimated. Some paths had portions lying on the boundary of the measured field. The outer path in these cases was not moved beyond the boundary. Similarly, some paths had fewer than two nodes between two sides of the path. In these cases, the inner paths were not moved inwards in that direction.

Because the resolution was relatively low in these measurements owing to experimental constraints, the error estimated in this way is quite large. This does not, however, affect the experimental findings, which we now summarize. It has been shown that streamwise vortex tubes are severely weakened in regions of locally stable stratifications. The value of Γ / Γ_{KH} at $x/\theta_0 = 70$ for $Ri_0 = 0$ was -8.2×10^{-2} . Using a smaller circuit gives a value of -6.1×10^{-2} . No outer path was used in this case, since the chosen path lies entirely on the boundary. For $Ri_0 = 0.06$, the circulation was 1.5×10^{-2} , a positive number. The value for the inner path was 1.4×10^{-3} and for the outer path was 1.9×10^{-2} . Despite the possible error, the trend remains clear.

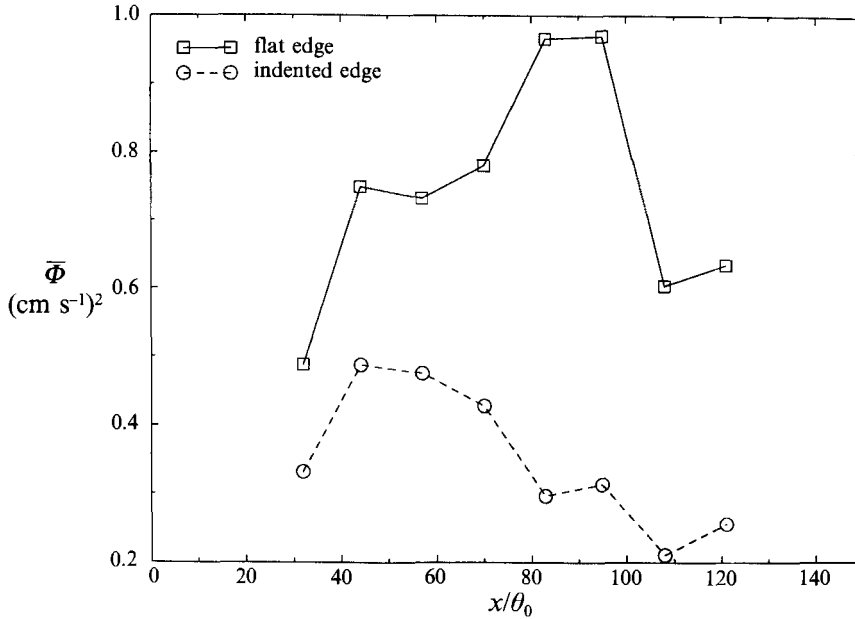


FIGURE 30. Potential energy development for $Ri_0 = 0.06$ with straight and indented splitter plate trailing edges.

It has also been shown that vortex tubes increase in strength in regions of locally unstable stratification. For $Ri_0 = 0$ at $x/\theta_0 = 83$, the circulation in this region was negligibly small, 0.25×10^{-2} . The inner path in this case gave a value of 5.2×10^{-4} . The larger circuit probably encloses part of the nearby opposite-sign vortex tube, since the integration around this path yielded $\Gamma/\Gamma_{KH} = -0.5 \times 10^{-2}$. In the stratified case ($Ri_0 = 0.06$), we found a dimensionless strength of 4.6×10^{-2} with 3.7×10^{-2} for the slightly smaller circuit and 2.8×10^{-2} for the larger one. These values are all significantly larger than the $Ri_0 = 0$ case.

An increase in the absolute value of the baroclinically generated vortices was observed between the two downstream measurement locations for $Ri_0 = 0.06$. At $x/\theta_0 = 70$, Γ/Γ_{KH} was found to be -1.2×10^{-2} . A smaller path gave -0.14×10^{-2} and a larger one gave -4.2×10^{-6} . This larger path includes some of the vorticity from the tube which has changed sign, thus yielding a smaller absolute result. At $x/\theta_0 = 83$, the vortex strength was -3.5×10^{-2} . For the inner circuit, $\Gamma/\Gamma_{KH} = -1.8 \times 10^{-2}$, while for the outer circuit -2.5×10^{-2} . All of these are larger in magnitude than the upstream values.

For $Ri_0 = 0.089$, a decreasing trend in baroclinically generated vortex strength was observed with downstream distance. At $x/\theta_0 = 70$, we observed a circulation of -3.4×10^{-2} . An inner circuit gave -2.1×10^{-2} and an outer one gave -1.9×10^{-2} . At $x/\theta_0 = 83$, $\Gamma/\Gamma_{KH} = -1.4 \times 10^{-2}$ for the chosen path, -0.33×10^{-2} for the smaller circuit, and -0.60×10^{-2} for the larger. Thus, again, the trend is significant.

We now turn to a simple numerical model to understand better the physics behind the trend of decreasing tube strength under locally stable stratification and the trends in the growth of the baroclinically generated vortices.

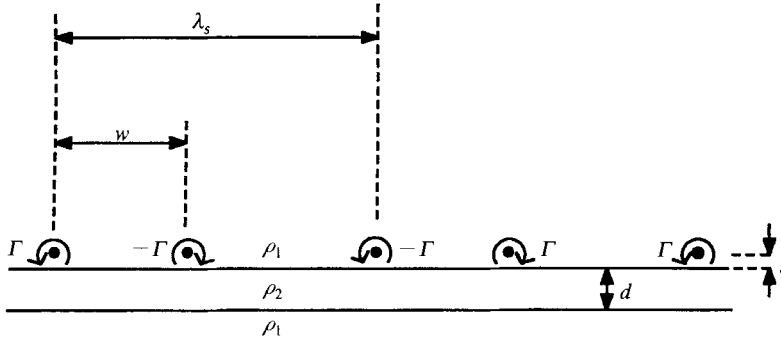


FIGURE 31. Conceptual model of heavy fluid layer and streamwise vortices.

4. Numerical modelling of the buoyancy-induced instability

4.1. Model description

In order to support qualitatively the interpretations of §3.3.2, a model containing the essential physics of the problem has been constructed. Fundamentally, we want to observe the evolution of a layer of high-density fluid, surrounded by low-density fluid when perturbed by an infinite row of counter-rotating vortex pairs near the upper interface. This configuration is shown in figure 31. The heavy layer represents the overturn above the Kelvin–Helmholtz core and the row of counter-rotating vortices represents the streamwise vortex tubes formed as a result of the imposed spanwise perturbation of the indented splitter plate. λ_s represents the spanwise wavelength, w the distance between the pairs of vortices marking the boundaries of the upwelling region (the area where the net induction is upward), s the initial spacing between the streamwise vortex tubes and the top interface, and Γ is the absolute value of the streamwise vortex strength.

Aref & Tryggvason (1989) have described the use of variable circulation point vortices (not to be confused with those mentioned above) to model an inviscid immiscible density interface. In this method, the interface is split up into point vortices and passive markers placed between them. The purpose of the markers is to determine the slope of the interface at each vortex, thus enabling the calculation of the baroclinic torque and the adjustment of the vortex strength. For computational purposes, the passive points are given odd numbers and the active point vortices are given even numbers. This configuration is shown in figure 32 (note that, in this coordinate system, x is spanwise and y is vertical relative to the shear layer). The two-dimensional vorticity transport equation is now reduced to

$$\frac{d\Gamma_{2j}}{dt} = 2(y_{2j+1} - y_{2j-1}), \quad (4.1)$$

where j increases with x when the high-density fluid is above the interface, and j decreases with x when the low-density fluid is above the interface. Γ_{2j} is the circulation around the $2j$ th vortex, and y_{2j+1} and y_{2j-1} denote the y values for those passive points. All lengths are non-dimensionalized with λ_s and all times are scaled by $[\lambda_s[\rho_1 + \rho_2]/g[\rho_1 - \rho_2]]^{1/2}$. Because this timescale has a singularity when the two layers have equal densities, a different timescale (λ_s^2/Γ) must be used in the unstratified case. Assuming a periodic box of unit width, then, the points and the

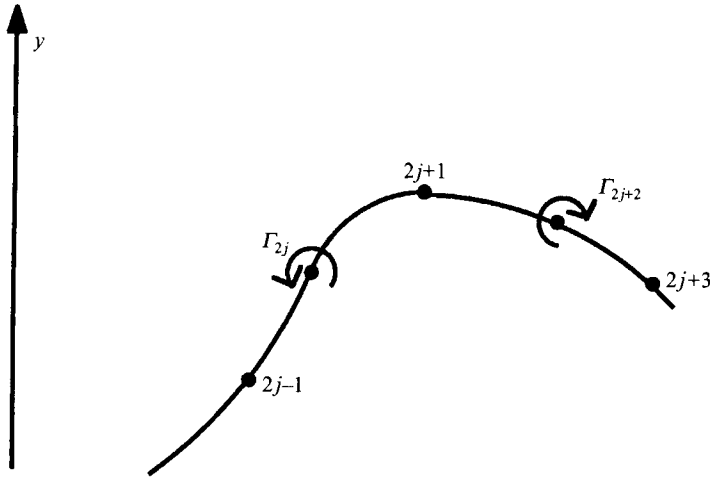


FIGURE 32. Configuration of points and vortices representing the interface in the numerical model.

vortices are advected with

$$\frac{d\bar{z}_j}{dt} = \frac{1}{2i} \sum_{k \neq j} \Gamma_k \cot\{\pi(z_j - z_k)\}, \quad (4.2)$$

where $z = x + iy$ and $\bar{z} = x - iy$. This expression is derived by considering the induction from each vortex in the periodic box, along with its infinity of images, one for each horizontal period. The expression for the complex potential of an infinite row of point vortices is given in Lamb (1932). For details of the derivation, see Schowalter (1993). At each time step, a second-order Runge–Kutta method is used to advect the points and (4.1) is used to adjust the strengths.

Because of the small-scale instabilities entailed in the evolution of a row of point vortices, we used Gaussian vortex ‘blobs’ instead. This method is described in detail by Nakamura, Leonard & Spalart (1982) for simulating a constant-density two-dimensional shear layer. When calculating the advecting velocity at one point due to a vortex and its periodic images, the vortex itself is modelled as having a Gaussian distribution of vorticity and its images, being much further away, are modelled as point vortices. Thus, the induced velocities given by (4.2) are altered to

$$\frac{d\bar{z}_j}{dt} = \frac{1}{2i} \sum_{k \neq j} \left\{ -\frac{\Gamma_k}{\pi} \frac{\bar{z}_j - \bar{z}_k}{r^2} \exp\left(\frac{-r^2}{\sigma^2}\right) + \Gamma_k \cot(\pi[z_j - z_k]) \right\}, \quad (4.3)$$

where σ is the vortex blob radius and $r^2 = (x_j - x_k)^2 + (y_j - y_k)^2$. The additional term is the correction for treating the vortices within one horizontal period as having a Gaussian distribution. This Gaussian distribution was used for the interfacial vortices and for the vortex tubes lying above the overturn, the latter having a much larger radius than the former.

Although it would be a simple matter to allow viscous diffusion of the vortex tubes in the model, this would add considerable complication for the vortices representing the interface. The difficulty arises due to the changing circulation of the latter vortices. Because it would be inconsistent to allow diffusion of only some of the vorticity in the flow, none has been included.

4.2. Numerical results

4.2.1. Rayleigh–Taylor instability

The model was first tested by simulating a Rayleigh–Taylor instability. Thus, there is only one interface separating an upper semi-infinite region of high-density fluid from a lower semi-infinite region of low-density fluid. The interface was given an initial sinusoidal perturbation. The effective interfacial thickness is given by the diameter of the interfacial vortex blob radius. The exponential growth rate of the maximum displacement of the interface versus dimensionless time for varying interfacial thickness, δ , is shown in figure 33. The curves reveal a linear regime, in which the growth rate is nearly constant, a nonlinear regime, in which the growth rate decreases at later time, and a pre-linear regime at small times. The pre-linear regime is due to the initial conditions having a perturbation in interface position, but no perturbation in initial interfacial vorticity. Thus, the vorticity amplitude takes some time to catch up to the interfacial position amplitude. The linear growth rate can be seen to depend upon the interfacial thickness. The theoretical linear growth rate for an infinitely thin interface (see Drazin & Reid 1981), after non-dimensionalization, is $(2\pi)^{1/2}$, or about 2.507, and the curves approach that value as the thickness decreases. The experimental interfacial thickness at $x/\theta_0 = 70$ can be estimated by molecular diffusion as being about 0.0015, when non-dimensionalized by the spanwise wavelength. The simulated value of 0.0088 is thus of the same order of magnitude. The vortex blob radius used in this case was large enough to maintain stability for the calculations, and the number of points used (512 per interface from $x = 0$ to $x = 0.5$) allowed the calculations to be accomplished in a reasonable amount of time. To maintain stability and to decrease blob size further would have required more interfacial vortices. As the simulation time increases as the number of points squared, it was impractical to add more points. It should be mentioned that the development of the interfaces was essentially unchanged when twice as many vortices were used with the same interfacial thickness.

4.2.2. Results with no stratification

For comparison with experimental results at $Ri_0 = 0$, the simulation was run with only passively advecting points on the interfaces. Since there were no density differences in this case, time is scaled with λ_s^2/Γ , where Γ is the circulation of the vortex tubes. Figure 34 shows the development of the overturn with variables chosen to mimic the experimental case. An asterisk denotes non-dimensionalization. Dimensionless tube core radius (r_t^*) and initial tube-interface separation (s^*), two values which could not be measured in the experiment, were chosen to be 0.05 and 0.01, respectively. Comparison of figure 34 (c) with figure 10 reveals that the essential physics of the upwelling region between the vortex tubes has been captured by the unstratified model. The distortion of the overturn in the downwelling region is caused by the wrapping of the lower vortex tubes under the spanwise roller. Neither the lower vortex tubes nor the roller are included in the model.

4.2.3. Results with stratification

For the stratified version of the model, we start with parametric values which qualitatively correspond to the experimental conditions of the $Ri_0 = 0.06$ case. As an initial value of the vortex tube strength we use the circulation measured at $x/\theta_0 = 70$ in the *unstratified* case, the assumption being that the vortex tube is initially stretched and enhanced in the same manner, stratification only affecting its development afterwards.

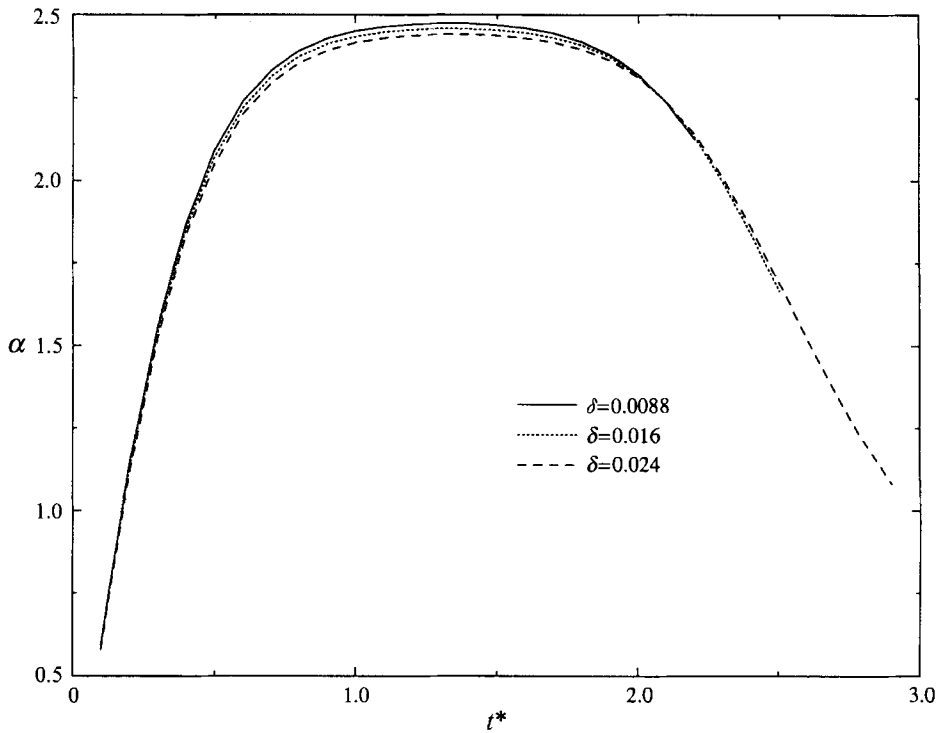


FIGURE 33. Exponential growth rate of Rayleigh–Taylor instability for various interfacial thicknesses using numerical model.

Figure 35 shows the interfacial position at various dimensionless times for this case. As with t^* , Γ^* denotes non-dimensionality. At $t^* = 0.50$, we can clearly observe the baroclinically generated vortices which occur experimentally. They seem to be at a higher vertical position, however, and in general there seems to be more heavy fluid pulled upward by the streamwise vortex tubes than in the experimental case. The simulation was run with many variations of the parameters and we found that the case which most visually resembled the experiment had a smaller tube strength and a smaller tube radius than that shown in figure 35. This is shown in figure 36, where the dimensionless circulation is 0.08, compared to 0.18 for figure 35. In addition, the tube radius has been decreased from 0.05 to 0.03. Here we see development very similar to that in the current experiments. Only thin wisps of heavy fluid are pulled over the vortex tubes and baroclinic vortices form on the lower interface which was initially tilted by the tubes. It is useful to compare this figure with figure 12 (*a*). One structural difference between the model and the experiment is the small vortex which forms at the base of the wisp which is pulled over the vortex tube in the model. Perhaps this does not form in the experiment because there is enough viscous diffusion between the interface vorticity and the tube vorticity that there is never a high enough vorticity concentration to have a roll-up there. The model contains no diffusion.

Thus, it seems that vortex tube weakening may be more dramatic in the experiment than in the model. Vortex tube strength evolution is shown in figure 37 for all parametric variations. Here Γ_0 is the initial vortex tube strength and Γ is the total circulation contained within the vortex tube radius at varying times. There are large variations in the development for different cases, but the most extreme

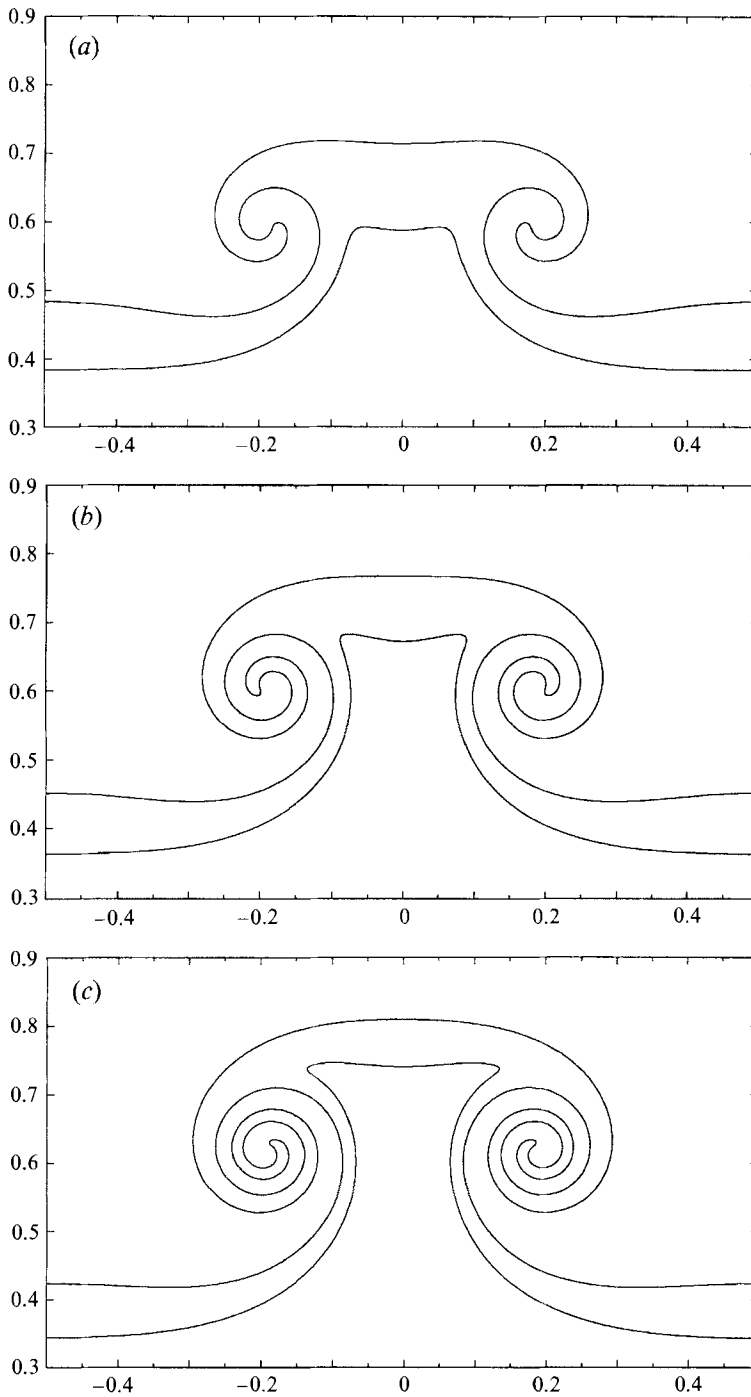


FIGURE 34. Interfacial position from simulation of unstratified overturn. $d^* = 0.12$, $r_l^* = 0.05$.
(a) $t^* = 0.120$. (b) $t^* = 0.180$. (c) $t^* = 0.240$.

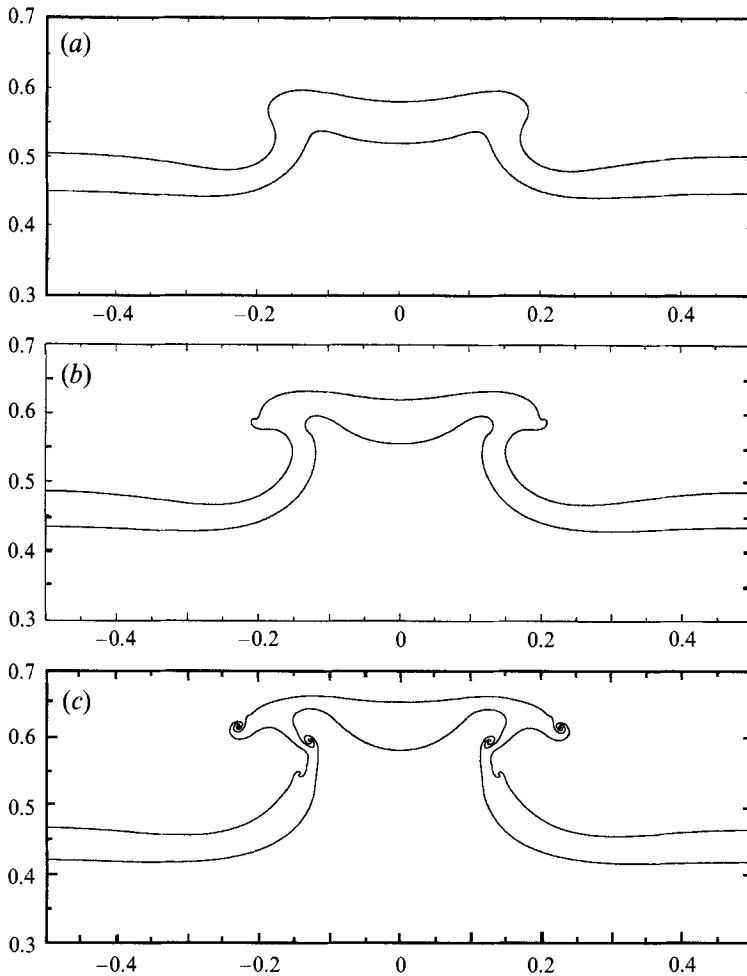


FIGURE 35. Interfacial position from simulation of stratified overturn. $d^* = 0.057$, $r_i^* = 0.05$, $\Gamma^* = 0.18$. (a) $t^* = 0.20$. (b) $t^* = 0.35$. (c) $t^* = 0.50$.

weakening results in the tube strength being 60% of its original value. Remember that, experimentally, it was found that the stratification could actually reverse the sign of the tube circulation. For many of the model cases, the strength actually rises at later times. In these cases, the lower interface vorticity, having the same sign as the local tube vorticity, is entrained into the Gaussian core of the vortex tube, resulting in a larger circulation within the core. In any case, the model does not seem to sufficiently describe the vortex tube weakening seen experimentally. We speculate that this is the reason for needing to use a smaller initial tube strength in order to get qualitative agreement with experimental observations.

It is informative to compare model development times with experimental values. We note that the simulation results shown in figure 36 appear most like the end view image shown in figure 12 at $t^* = 0.45$. Using the roller convective velocity $\frac{1}{2}(U_1 + U_2)$ and non-dimensionalizing, we can calculate the dimensionless time for the experimental image after which overturn first occurred. Using this method, we get a value of $t^* = 0.99$ for the images in figure 12, roughly twice the value for the model,

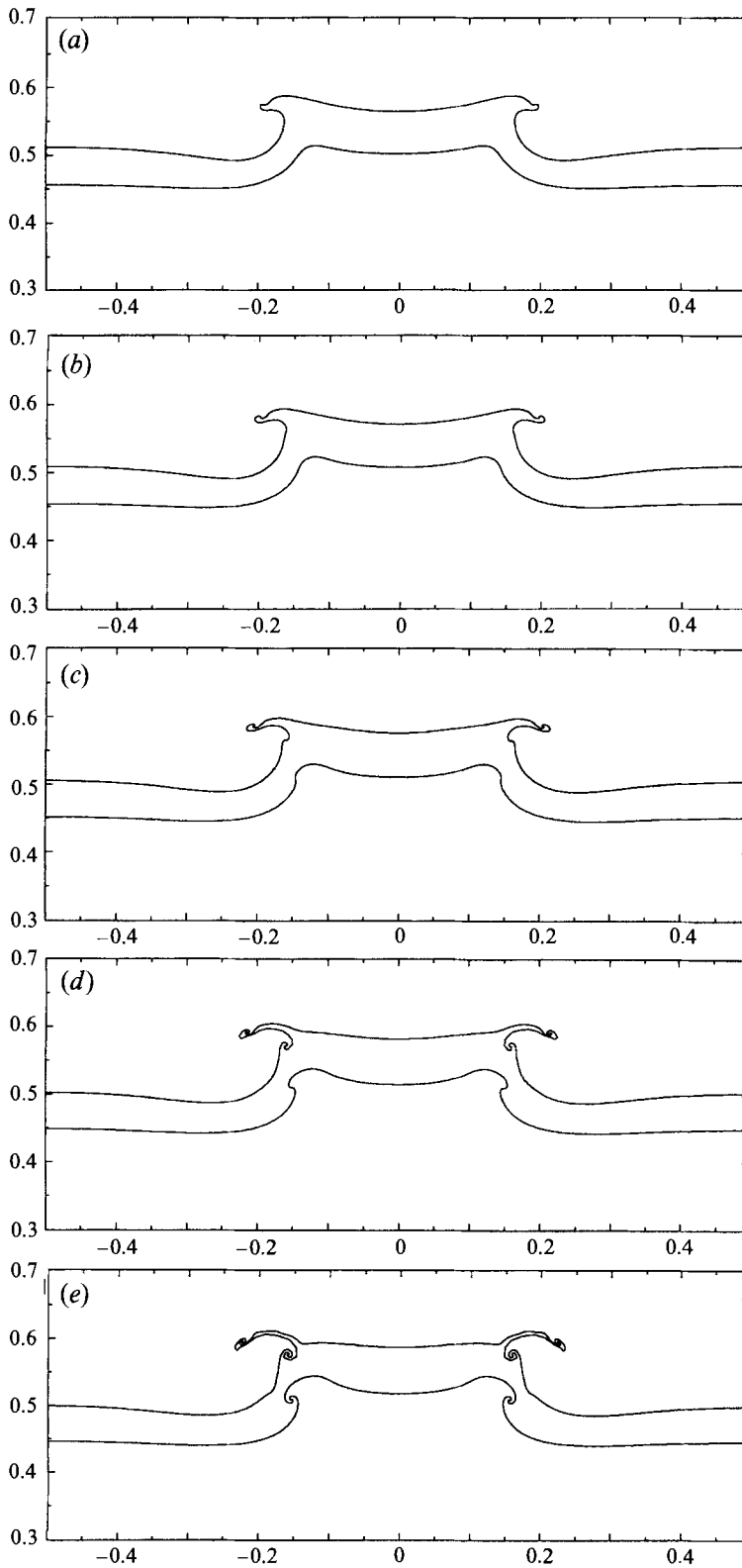


FIGURE 36. For caption see facing page.

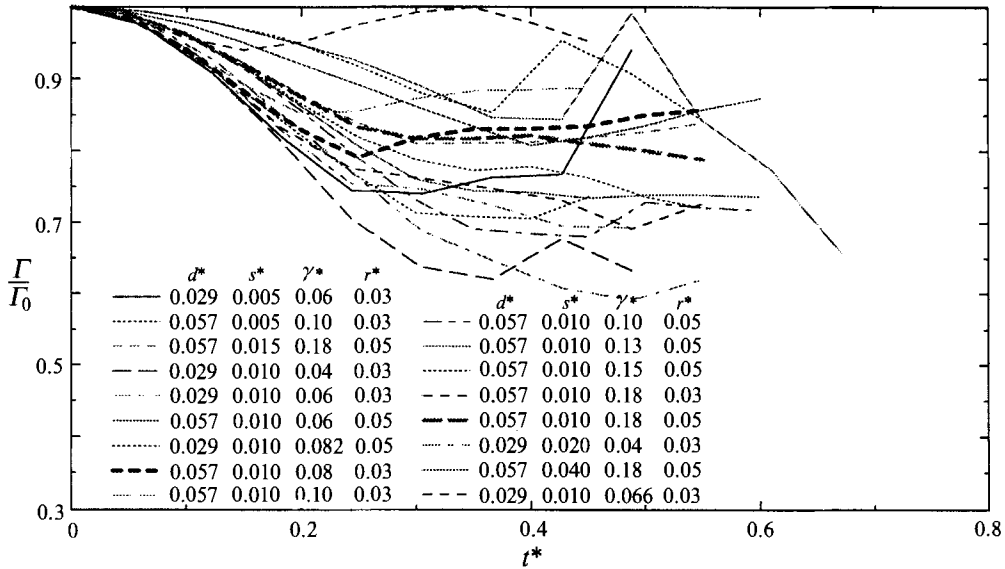


FIGURE 37. Time evolution of circulation within vortex tube for all simulations. The thick lines represent the simulations depicted in figures 35 and 36.

even though they seem to be at the same stage of development. Thus, the model vortices develop more rapidly than in the experiment. This is perhaps not surprising when one considers that the experimental vortex tube may not be fully stretched nor contain all of its braid vorticity when overturning first occurs. The vortex tube is probably stretching and acquiring vorticity from the braid at this time so that the fluid is not initially subjected to as strong an upwelling as in the model, leading to a longer development time for the experimental case.

Figure 38 shows the exponential growth rate versus dimensionless time for the baroclinically generated vortices for all of the simulations run. The simulation breaks down when interfaces cross one another due to finite resolution. To calculate the growth rate, the portion of the interface entrained in the vortex was determined at the last time before simulation breakdown. The total vorticity within this portion of the interface was then computed from $t^* = 0.05$ to the time of simulation breakdown. α is the growth rate of the circulation within this section of the interface.

At small times, α is much larger than $(2\pi)^{1/2}$, the growth rate for the Rayleigh–Taylor instability. In that instability, exponential growth results from a perturbed interface causing baroclinic generation of vorticity on the interface, resulting in further sloping of the interface, stronger baroclinic generation, and so on. In the case of the roller-induced overturn, the distortion of the interface is caused not only by the vorticity on the interface, but by the streamwise vortex tubes. Thus, the growth rate is considerably larger. In this initial growth period, there is very little differentiation between the various simulations. At later times, however, the curves begin to move apart. The curve with the lowest growth rate occurs for a dimensionless tube radius of 0.03 and a dimensionless tube circulation of 0.18. Here,

FIGURE 36. Interfacial position from simulation of stratified overturn. $d^* = 0.057$, $r_i^* = 0.03$, $\Gamma^* = 0.080$. (a) $t^* = 0.30$. (b) $t^* = 0.35$. (c) $t^* = 0.40$. (d) $t^* = 0.45$. (e) $t^* = 0.50$.

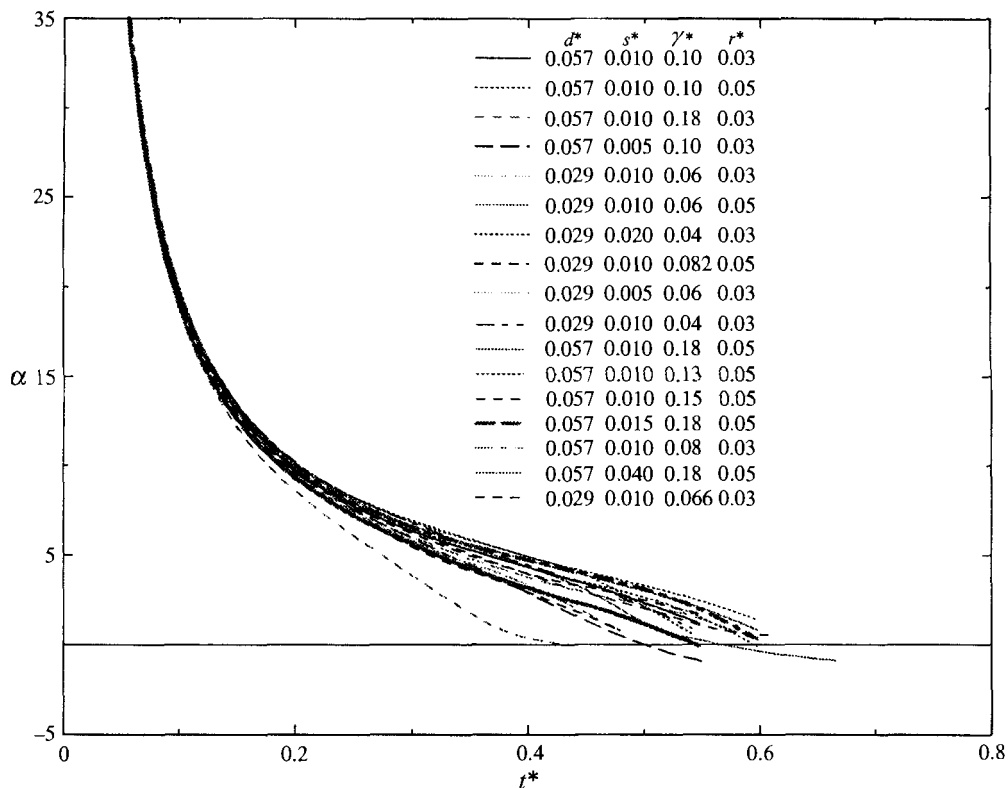


FIGURE 38. Time evolution of growth rate of baroclinically generated vortices for all simulations. The thick lines represent the simulations depicted in figures 35 and 36.

the baroclinically generated vortices are advected over the vortex tubes before getting a chance to grow appreciably. Some curves do actually cross the t^* axis before breakdown, resulting in a negative growth rate. This important result agrees with the experimental observation of eventual vortex weakening in § 3.3.2. Since the curves in figure 38 collapse, the timescale for baroclinic vortex development can be considered to be $(\lambda_s[\rho_1 + \rho_2]/g[\rho_1 - \rho_2])^{1/2}$, the temporal non-dimensionalization factor for the model. Thus, if the time were dimensionalized, the curves representing the higher Richardson number case would be shifted to the left of the curves representing the lower Richardson case. The baroclinically generated vortices gain strength more quickly and subsequently lose strength more quickly for the higher Richardson number, since Richardson number is proportional to density difference between layers. It follows that, at an upstream measurement position, the baroclinic vortex strength would be higher for the higher Richardson number, but at a downstream measurement position, the lower Richardson number baroclinic vortex would have the greater strength. The circulation of the baroclinic vortices eventually decreases because, as heavy fluid winds around, the baroclinic generation changes sign. The draining of heavy fluid above the region of vortex formation, however, may be an additional contribution to this weakening process. For example, in figure 22, it can be seen that the baroclinic vortex does not have many windings, but there is very little heavy fluid remaining in the layer above the vortex. This weakening does not mean the end of streamwise vortices altogether, however. As long as there is heavy

fluid above light fluid, there exists potential energy for the creation of vorticity. New generations of vortices will continue to form until the stratification becomes stable. One would imagine that a considerable amount of mixing would take place throughout this process. Perhaps this mechanism replaces the 'mixing transition' route to turbulence observed in homogeneous shear layers.

5. Conclusions

The effect of stratification on streamwise vortex structure in the shear layer has been investigated experimentally through the use of fluorescence visualization and laser-Doppler anemometry. A two-dimensional vortex dynamics model has been used to aid physical understanding of the experimental results. It has been found that stratification produces several important effects on three-dimensional shear layer development, which are outlined below.

Streamwise vortex tubes resulting from the stretching of braid vorticity are weakened by locally stable stratification and enhanced by locally unstable stratification. It should be noted that, without stratification, these tubes are strongest in the braid region and where they extend directly from the braid to the regions above and below the spanwise cores. This is where there is locally stable stratification for positive initial Richardson numbers, and where they become weakened by baroclinically generated vorticity of opposite sign. This was shown by experimental data and through numerical modelling, though the modelling results do not show the dramatic weakening that was observed experimentally. In the unstratified case, only weak vorticity exists where the hairpins are partially entrained into the core. They are strengthened here by locally unstable stratification for positive Ri_0 . This was shown experimentally, particularly in the bottom half of the spanwise roller core.

High-density fluid is pulled above low-density fluid in the initial roll-up of the spanwise cores. Klaassen & Peltier (1985a) showed that this region is dynamically unstable in the linear regime. The current experimental evidence supports that claim and shows continued instability into the nonlinear regime, resulting in baroclinically generated streamwise vortices. Experimental data and modelling results show that the streamwise vortex tubes resulting from the stretching of braid vorticity enhance the growth of these buoyancy-induced vortex structures by causing large spatial perturbations in the unstable density interface. Owing to this interaction, the baroclinically generated vortices have a much higher initial growth rate than a Rayleigh–Taylor instability. This growth rate eventually decreases, however, becoming negative as the vortex weakens. Development time scales as $(\lambda_s[\rho_1 + \rho_2]/g[\rho_1 - \rho_2])^{1/2}$. Thus, for a higher initial Richardson number (higher density difference), the growth rate will be higher initially, but weakening will also occur at an earlier time (further upstream).

The conclusions regarding the relative strength of vortices for varying stratification and downstream position are based upon visualization, circulation calculation, and modelling results. Although there is some error associated with the second of these, it was shown in §3.5 that this error does not affect the conclusions about general trends.

Even for $Ri_0 = 0.03$, the smallest non-zero Richardson number experimentally investigated, the buoyancy-induced streamwise vortices eventually dominate the flow structure. For higher initial Richardson numbers, this domination occurs further upstream. In addition, we have seen that the presence of these vortices results in a more rapid conversion of potential energy into kinetic energy, possibly resulting in an earlier transition to turbulence.

In the future, it would be informative to use spanwise forcing of varying wavelength, thus observing the effect of wavelength on the growth rate of the baroclinically generated vortices. It will be important, however, to differentiate between the wavelength effect on the vortex tube formation and the wavelength effect on the baroclinic vortex development.

The work presented here is the product of the primary author's PhD thesis. We would like to acknowledge the suggestions of Professor Constantine Pozrikidis regarding the numerical model. Financial support was given by the Office of Naval Research under contract # N00014-92-J-1121 and by the National Science Foundation under grant OCE 92-17213.

REFERENCES

- AREF, H. & TRYGGVASON, G. 1989 Model of Rayleigh–Taylor instability. *Phys. Rev. Lett.* **62**, N7, 749.
- BARRETT, T. K. & VAN ATTA, C. W. 1991 Experiments on the inhibition of mixing in stably stratified decaying turbulence using laser Doppler anemometry and laser-induced fluorescence. *Phys. Fluids A* **3**, 1321.
- BERNAL, L. P. & ROSHKO, A. 1986 Streamwise vortex structure in plane mixing layers. *J. Fluid Mech.* **170**, 499.
- BREIDENTHAL, R. 1981 Structure in turbulent mixing layers and wakes using a chemical reaction. *J. Fluid Mech.* **109**, 1.
- BROWAND, F. K. & WINANT, C. D. 1973 Laboratory observations of shear-layer instability in a stratified fluid. *Boundary-Layer Met.* **5**, 67.
- BROWN, G. L. & ROSHKO, A. 1974 On density effects and large structure in turbulent mixing layers. *J. Fluid Mech.* **64**, 775.
- DIMOTAKIS, P. E. & BROWN, G. L. 1976 The mixing layer at high Reynolds number: large-structure dynamics and entrainment. *J. Fluid Mech.* **78**, 535.
- DRAZIN, P. G. & REID, W. H. 1981 *Hydrodynamic Stability*, chap 1. Cambridge University Press.
- FARMER, D. M. & ARMI, L. 1988 The flow of Atlantic Water through the Strait of Gibraltar. *Prog. Oceanogr.* **21**, 1.
- GARTRELL, G. 1979 Studies on the mixing in a density-stratified shear flow. PhD thesis, Division of Engineering and Applied Science, California Institute of Technology.
- HANNOUN, I. A. 1985 Matching the refractive index in density stratified flows. *W.M. Keck Laboratory of Hydraulics and Water Resources Tech. Mem.* 85-1. California Institute of Technology.
- JIMENEZ, J. 1983 A spanwise structure in the plane shear layer. *J. Fluid Mech.* **132**, 319.
- KLAASSEN, G. P. & PELTIER, W. R. 1985a The onset of turbulence in finite-amplitude Kelvin–Helmholtz billows. *J. Fluid Mech.* **155**, 1.
- KLAASSEN, G. P. & PELTIER, W. R. 1985b The effect of the Prandtl number on the evolution and stability of Kelvin–Helmholtz billows. *Geophys. Astrophys. Fluid Dyn.* **32**, 23.
- KLAASSEN, G. P. & PELTIER, W. R. 1991 The influence of stratification on secondary instability in free shear layers. *J. Fluid Mech.* **227**, 71.
- KONRAD, J. H. 1976 An experimental investigation of mixing in two-dimensional turbulent shear flows with applications to diffusion-limited chemical reactions. *Project SQUID Tech. Rep.* CIT-8-PU.
- KOOP, C. G. & BROWAND, F. K. 1979 Instability and turbulence in a stratified fluid with shear. *J. Fluid Mech.* **93**, 135.
- LAMB, H. 1932 *Hydrodynamics*, chap. 7. Dover.
- LASHERAS, J. C. & CHOI, H. 1988 Three-dimensional instability of a plane free shear layer: an experimental study of the formation and evolution of streamwise vortices. *J. Fluid Mech.* **189**, 53.
- LAWRENCE, G. A., LASHERAS, J. C. & BROWAND, F. K. 1987 Shear instabilities in stratified flow. *Third Intl Symp. on Stratified Flows*, 2360.
- LIEPMANN, H. W. & LAUFER, J. 1947 Investigation of free turbulent mixing. *NACA Tech. Note* 1257.

- LIN, S. J. & CORCOS, G. M. 1984 The mixing layer: deterministic models of a turbulent flow. Part 3. The effect of plane strain on the dynamics of streamwise vortices. *J. Fluid Mech.* **141**, 139.
- MARMORINO, G. O. 1987 Observations of small-scale mixing processes in the seasonal thermocline, part II: wave breaking. *J. Phys. Oceanogr.* **17**, 1348.
- MCDUGALL, T. J. 1979 On the elimination of refractive-index variations in turbulent density stratified liquid flows. *J. Fluid Mech.* **93**, 83.
- NAKAMURA, Y., LEONARD, A. & SPALART, P. 1982 Vortex simulation of an inviscid shear layer. *AIAA/ASME 3rd Joint Thermophysics, Fluids, Plasma and Heat Transfer Conference, St. Louis. AIAA-82-0948.*
- ORLANSKI, I. & BRYAN, K. 1969 Formation of the thermocline step structure by large amplitude internal gravity waves. *J. Geophys. Res.* **74**, 6975.
- PATNAIK, P. C., SHERMAN, F. S. & CORCOS, G. M. 1976 A numerical simulation of Kelvin–Helmholtz waves of finite amplitude. *J. Fluid Mech.* **73**, 215.
- ROGERS, M. M. & MOSER, R. D. 1992 The three-dimensional evolution of a plane mixing layer: the Kelvin–Helmholtz rollup. *J. Fluid Mech.* **243**, 183.
- SCHOWALTER, D. G. 1993 The effect of stable stratification on three-dimensional structure in shear layers. PhD dissertation, Department of Applied Mechanics and Engineering Sciences, University of California, San Diego.
- STAQUET, C. 1989 Influence of a shear on a stably-stratified flow. *Turbulence and Coherent Structures: Selected papers from "Turbulence 89: Organized Structures and Turbulence in Fluid Mechanics," Grenoble, 18-21 September 1989.*
- STAQUET, C. & RILEY, J. J. 1989 On the velocity field associated with potential vorticity. *Dyn. Atmos. Oceans* **14**, 93.
- THORPE, S. A. 1985 Laboratory observations of secondary structures in Kelvin–Helmholtz billows and consequences for ocean mixing. *Geophys. Astrophys. Fluid Dyn.* **34**, 175.
- THORPE, S. A., HALL, A. J., TAYLOR, C. & ALLEN, J. 1977 Billows in Loch Ness. *Deep-Sea Res.* **24**, 371.
- WINANT, C. D. & BROWAND, F. K. 1974 Vortex pairing: the mechanism of turbulent mixing-layer growth at moderate Reynolds number. *J. Fluid Mech.* **63**, 237.
- WOODS, J. D. 1968 Wave-induced shear instability in the summer thermocline. *J. Fluid Mech.* **32**, 791.